Electrocatalytic Water Oxidation by a Trinuclear Copper(II) Complex

Ana M. Geer[†], Charles Musgrave[‡], Christopher Webber[†], Robert J. Nielsen[‡], Bradley A. McKeown[†], Chang Liu[†], P. Philipp M. Schleker[§,%], Peter Jakes[%], Xiaofan Jia[†], Diane A. Dickie[†], Josef Granwehr,[%] Sen Zhang[†], Charles W. Machan[†]*, William A. Goddard III[‡]*, T. Brent Gunnoe[†]*

[†]Department of Chemistry, University of Virginia, Charlottesville, VA 22904

[‡]Materials and Process Simulation Center, Department of Chemistry, California Institute of Technology, Pasadena, CA 91125

[§]Department of Heterogeneous Reactions, Max Planck Institute for Chemical Energy Conversion, 45470 Mülheim an der Ruhr, Germany
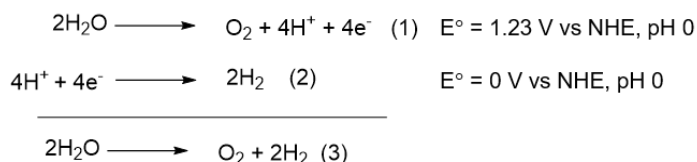
[%]Institute for Energy and Climate Research - Fundamental Electrochemistry (IEK-9), Forschungszentrum Jülich, 52425 Jülich, Germany

Abstract

We report a trinuclear copper(II) complex, $[(DAM)Cu_3(\mu^3\text{-}O)][Cl]_4$ (**1**, DAM = dodecaaza macrotetracycle), as a homogeneous electrocatalyst for water oxidation to dioxygen in phosphate-buffered solutions at pH 7.0, 8.1 and 11.5. Electrocatalytic water oxidation at pH 7 occurs at an overpotential of 550 mV with a turnover frequency (TOF) of ~10 s^{-1} at 1.5 V vs NHE. Controlled potential electrolysis experiments at pH 11.5 over 3 h at 1.2 V and at pH 8.1 for 40 min at 1.37 V vs NHE confirm the evolution of dioxygen with Faradaic efficiencies of 81% and 45%, respectively. Rinse tests conducted after CPE studies provide evidence for the homogenous nature of the catalysis. The linear dependence of the current density on the catalyst concentration indicates a likely first-order dependence on the Cu precatalyst **1**, while kinetic isotope studies (H_2O versus D_2O) point to involvement of a proton in or preceding the rate determining step. Rotating ring-disk electrode measurements at pH 8.1 and 11.2 show no evidence of H_2O_2 formation and support selectivity to form dioxygen. Freeze-quench EPR studies during electrolysis provide evidence for the formation of a molecular copper intermediate. Experimental and computational studies support a key role of the phosphate as an acceptor base. Moreover, DFT calculations highlight the importance of second-sphere interactions and the role of the nitrogen-based ligands to facilitate proton transfer processes.

Introduction

Society depends on fossil fuels for energy production, but combustion of hydrocarbons produces CO_2, a known greenhouse gas, as a waste product.[1] Therefore the development of sustainable energy production based on carbon-neutral sources is of continuing interest.[1, 2] Artificial photosynthesis, which converts renewable energy sources to chemical fuels is a promising alternative to the use of fossil fuels.[3-5] The most direct chemical process for artificial photosynthesis of chemical fuels is net water splitting to form dihydrogen and dioxygen; the two half reactions for water splitting are the hydrogen evolution reaction (HER; cathodic process) and the oxygen evolution reaction (OER; anodic process) (Figure 1). The complexity of the water oxidation reaction, in which four electrons and four protons are transferred with the formation of an oxygen-oxygen multiple bond, results in kinetic challenges for selectivity.[6] A specific obstacle is the formation of metal oxo intermediates, which are important for the ultimate formation of the O–O bonds, as they are often stable, which can slow or prevent catalytic turnover.[7, 8] In nature, multi-electron and multi-proton processes are accomplished by enzymes whose active sites are commonly multinuclear clusters. For example, in photosystem II, the oxygen evolving complex (OEC) contains a Mn_4CaO_5 cluster responsible for water splitting and dioxygen evolution, which overcomes the challenge of the multi-electron water oxidation by accumulation of redox equivalents across the four manganese centers.[9-14] Despite intense study and significant fundamental advancements focused on catalytic materials for electrocatalytic water oxidation, this reaction remains one of the foremost challenges in molecular chemical catalysis.[5, 6, 15-17]

$$2H_2O \longrightarrow O_2 + 4H^+ + 4e^- \quad (1) \quad E° = 1.23 \text{ V vs NHE, pH 0}$$

$$4H^+ + 4e^- \longrightarrow 2H_2 \quad (2) \qquad E° = 0 \text{ V vs NHE, pH 0}$$

$$\overline{}$$

$$2H_2O \longrightarrow O_2 + 2H_2 \quad (3)$$

Figure 1. Overall water splitting reaction and half-reactions.

In the last decade, there has been increased interest in molecular catalysts for electrocatalytic water oxidation that are based on first-row transition metals.[6, 18-23] In particular, copper catalysts are of interest due to copper's earth abundance.[24, 25] Since Mayer and coworkers reported a molecular copper catalyst precursor for water oxidation in 2012,[26] additional progress has been made studying new molecular copper catalysts. Until recently, most copper mononuclear catalysts only operated under basic conditions (pH ≥ 8),[27-43] with limited examples of copper molecular catalysts at neutral pH.[44-48] Two copper complexes containing macrocyclic nitrogen-donor ligands,[44, 46] a copper(II) species that contains a substituted pyridyl(ethyl) amine ligand,[47] and a copper(II) complex with an aryl oxime ligand[45] catalyze water oxidation at pH 7 in phosphate buffer solution. Recently, Cao and coworkers have published a copper(II) porphyrin complex that catalyzes water oxidation at neutral pH and the two-electron oxidation of H_2O to H_2O_2 at pH 3. This is a rare example of a molecular copper catalyst for water oxidation that operates at pH < 7.[48]

Electrochemical water oxidation with molecular catalysts is proposed to occur mainly through two mechanisms − water nucleophilic attack (WNA) *via* a single-site mechanism, and the less commonly demonstrated interaction of two M–O units (I2M) where the coupling of two radical metal-oxyl centers to form an O–O bond occurs (Scheme 1).[49, 20, 50, 51, 47] Compared to mononuclear catalysts, multinuclear copper complexes can potentially access alternative reaction pathways, as it is conceivable that multiple metal centers can access cooperativity between the metal sites. That is, multinuclear copper complexes make attractive catalysts for water oxidation due to the possibility of delocalizing redox equivalents across the multiple metals and can be potentially advantageous for avoiding high-energy high-valent copper oxo species that are often proposed in single-site catalysis. In fact, for dinuclear copper compounds, cooperativity between two formally Cu^{III} centers for O–O bond formation has been proposed.[52, 53] Other unique mechanistic possibilities exist for multinuclear complexes: redox isomerization (RI) has been proposed for copper dinuclear catalysts.[42]
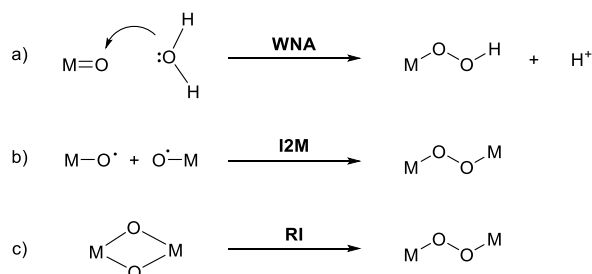

Scheme 1. Mechanisms for the formation of O−O bonds; a) water nucleophilic attack (WNA); M=O bond order is dependent on the d-electron count of the metal center and geometry. b) Interaction of two M–O species (I2M). c) Redox isomerization (RI) for dinuclear catalysts.

For context, the known multinuclear complexes most relevant to the trinuclear catalyst precursors studied herein will be discussed. A copper (II) dinuclear complex containing a naphthyridine ligand (**C**, Scheme 2) catalyzes electrochemical water oxidation at neutral pH with a TOF of 0.6 s^{-1} at 1 V overpotential.[52] DFT calculations predict that a pyridyl site in the ligand framework can act as an intramolecular proton acceptor; the pyridine is proposed to form a hydrogen bond with a hydroxyl ligand to facilitate intramolecular coupling in the formation of the O–O bond. A related unsymmetrical complex with one fewer pyridyl site requires buffer to assist the proton transfer, highlighting the potential role of the pyridyl ligand.[54] Another copper (II) dinuclear catalyst containing a tris(pyridylmethyl)amine ligand (**B**, Scheme 2) was found to oxidize water at basic pH (12.5) with a TOF of 33 s^{-1} at ~1 V overpotential.[42] A kinetic isotope effect (KIE) of 2.1(2) indicates the likelihood of a proton coupled electron transfer (PCET) as the rate limiting step,[55] and calculations support water nucleophilic attack on a dinuclear Cu(III) intermediate, $\{[LCu^{III}]_2\text{-}(\mu\text{-}O)_2\}^{2+}$, followed by redox isomerization. Dinuclear copper complexes with oxamide ligands (**A**, Scheme 2) were found to be active for both water oxidation and water reduction.[56, 57]

A recent study compares electrocatalytic water oxidation mediated by a dinuclear dipyridyl amino copper complex to the behavior of its analogous mononuclear species.[58] DFT calculations indicate

cooperation between the two copper centers of the dinuclear complex in the O−O bond formation step. Two trinuclear copper phosphonate complexes (as an example see **D**, Scheme 2) have been shown to be active electrocatalysts for water oxidation at neutral pH with low TOFs (0.58 and 0.82 s^{-1} at ~800 mV overpotential).[59] Inspired by the Mn_4CaO_5 site of the OEC, tetranuclear copper clusters have also been studied (for example, **E** and **F**, Scheme 2).[60-63] A complex with a chair-like Cu_4O_4 core is a water oxidation catalyst (WOC) at pH 7 with an overpotential of 730 mV.[60] Cubane-like Cu_4O_4 clusters are also active electrocatalysts for water oxidation at basic pH (12.0) with high catalytic activity (TOFs of 267 s^{-1} at 1.2 V overpotential and 105 s^{-1} at 1.1 V overpotential).[62] Based on Raman and electron paramagnetic resonance (EPR) data, the authors propose the Cu_4^{II} species is oxidized by two-successive 2e$^-$ oxidations to form an intermediate Cu_4^{III} species before reacting with hydroxyl.

Speculation that multi-nuclear Cu sites are important for recent reports of Cu/zeolite catalysts for thermal methane oxidation prompted our interest in multinuclear WOCs.[64-67] Thus, we sought a well-defined molecular trinuclear copper(II) complex, [(DAM)Cu$_3$(μ^3-O)][Cl]$_4$ (**1**, DAM = dodecaaza macrotetracycle), as a catalyst for electrocatalytic water oxidation. The experimental results indicate that complex **1** is active for electrocatalytic water oxidation with low catalytic onset potentials at pH 7.0, 8.1 and 11.5 and remains homogeneous in this pH range. High TOFs are obtained, 30.3 s^{-1} at pH 8.1 and 10.0 s^{-1} at pH 7 at ~800 mV overpotential. Moreover, both experimental and computational studies highlight the importance in the role of the buffer as a proton acceptor. DFT calculations indicate that the -NH groups of the ligand play a critical role as a proton shuttle.
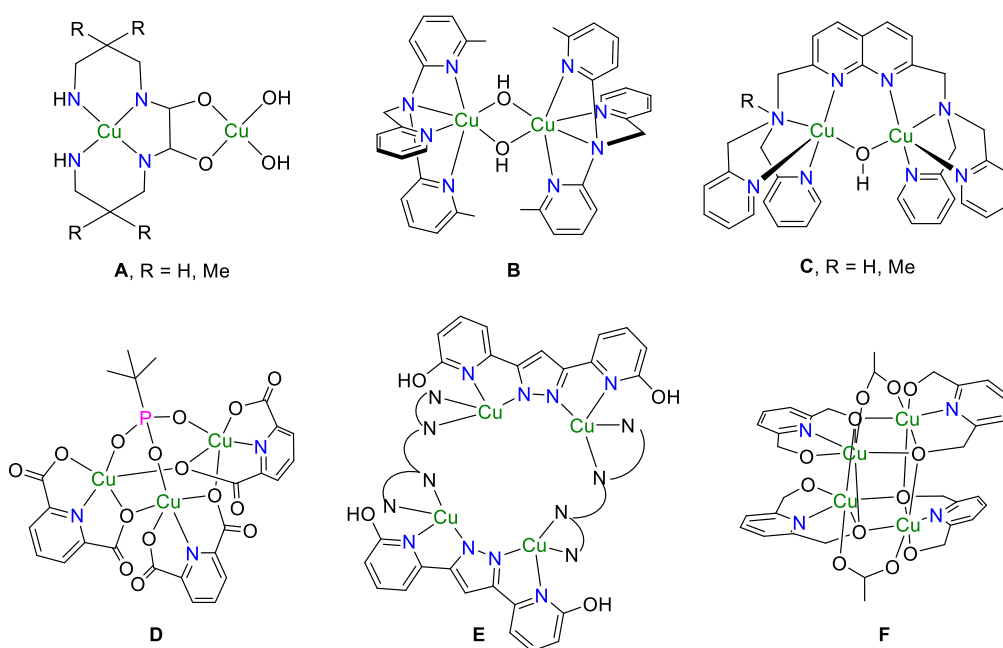
Scheme 2. Selected examples of multinuclear copper catalysts for electrochemical water oxidation. **A**: ref 56 and 57, **B**: ref 37, **C**: ref 52, **D**: ref 59, **E**: ref 61, **F**: ref 63.

Results and Discussion

Synthesis and Characterization

The trinuclear copper complex [(DAM)Cu$_3$(μ^3-O)][Cl]$_4$ (**1**) was synthesized with an isolated yield of 67% via a metal templated synthesis by a modification of a reported method.[68] The molecular structure was confirmed by single-crystal X-ray diffraction and features a (μ_3-oxo)Cu$_3$ core that adopts a molecular bowl shaped structure with each of the Cu(II) centers in a distorted trigonal bipyramid geometry with the μ^3-oxo and a tertiary nitrogen on the apical positions (Figure 2). The equatorial plane is occupied by two secondary amine nitrogen atoms and a tertiary amine nitrogen atom. The presence of the coordinated N–H groups are potentially important, as secondary-sphere interactions can have critical roles in redox catalysis and DFT calculations implicate this moiety in the mechanism for water oxidation (see below).[69] The μ^3-oxo ligand lies 0.560(2) Å above the Cu$_3$ plane with Cu–O bond distances of ~1.89 Å, similar to the reported structure with perchlorate counterions.[68] The UV-Vis spectrum of complex **1** in water and phosphate buffer shows a broad absorption band at 655 nm, characteristic of *d-d* transitions of the copper center (Figure S1).[70, 71]

3
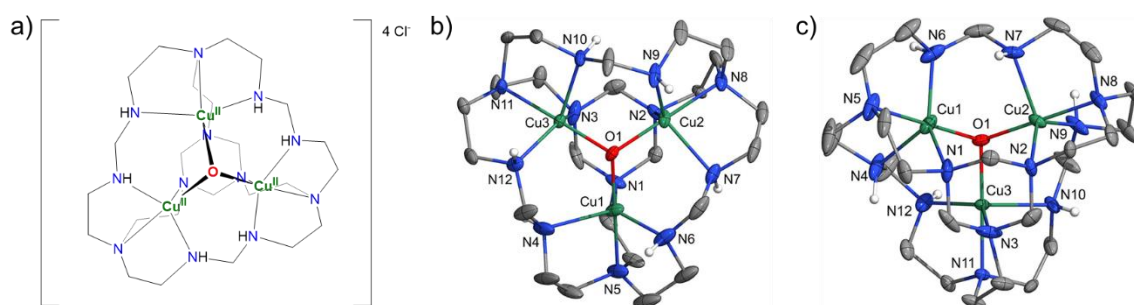
Figure 2. a) Model of the structure of [(DAM)Cu$_3$(μ_3-O)][Cl]$_4$ (**1**). b/c) Molecular structure (from single crystal X-ray diffraction study) with anisotropic displacement ellipsoids set at 50% probability. Hydrogen atoms and counterions have been omitted for clarity. Only the major position of the disordered atoms is shown. Selected bond distances (Å) and angles (°): Cu1-O1 1.8987(18), Cu1-N5 2.062(3), Cu1-N4 2.199(5), Cu1-N1 2.250(2), Cu1-N6 2.032(5), Cu1-N4A 2.074(6), Cu1-N6A 2.215(6), Cu2-O1 1.8960(19), Cu2-N8 2.048(3), Cu2-N7A 2.056(6), Cu2-N9 2.061(4), Cu2-N7 2.194(4), Cu2-N9A 2.211(6), Cu2-N2 2.252(2), Cu3-O1 1.8915(18), Cu3-N11 2.054(2), Cu3-N10A, 2.075(5), Cu3-N12 2.099(4), Cu3-N10 2.178(4), Cu3-N12A 2.207(5), Cu3-N3 2.229(2), Cu3-O1-Cu2 111.51(9), Cu2-O1-Cu1 111.60(9), Cu3-O1-Cu1 111.90(9).
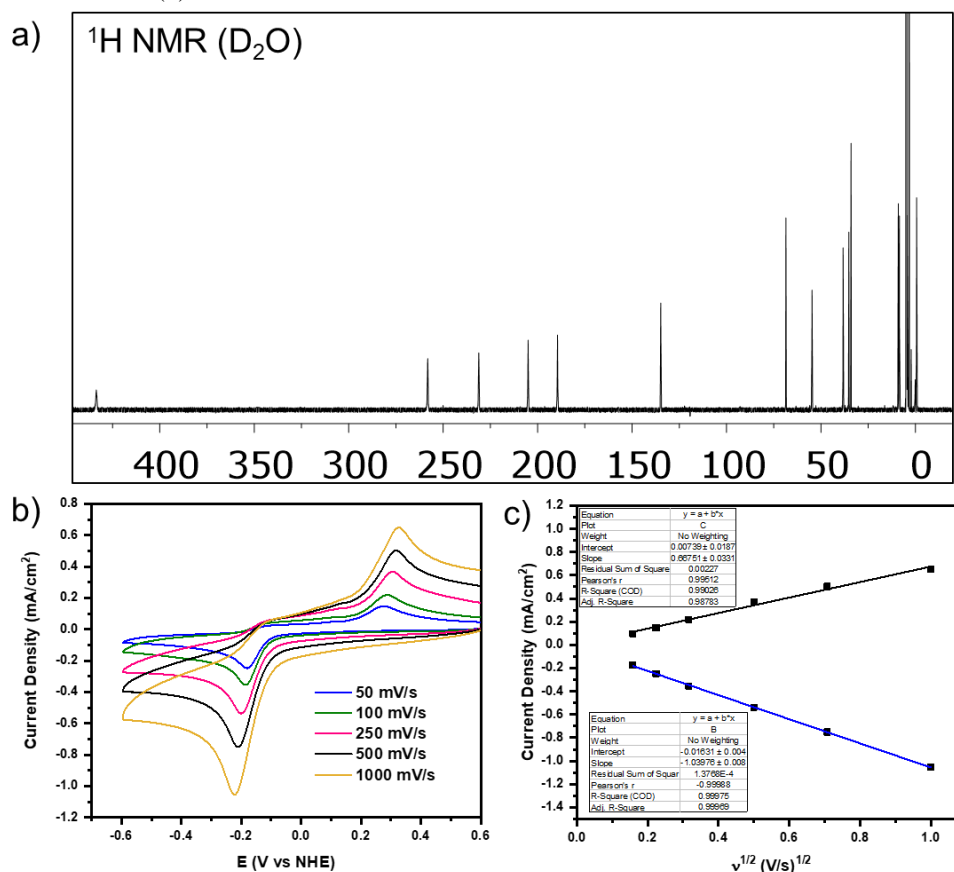

Figure 3. a) Wide-scan ^{1}H NMR spectrum of [(DAM)Cu$_3$(μ^3-O)][Cl]$_4$ (**1**) in D$_2$O. b) Cyclic voltammogram for complex **1** (0.5 mM) in 0.1 M phosphate buffer solution for scan rates of 50-1000 mV/s. c) Linear relation between the catalytic current density at E$_{p,c}$ = − 0.20 V (blue fit) and at E$_{p,a}$ = 0.29 V (black fit) and the square root of the scan rate ($v^{1/2}$) at pH 7 0.1 M phosphate buffer solution.

Wide-scan ^{1}H NMR spectroscopy in D$_2$O displays 15 broad paramagnetically shifted peaks from 434 to -1 ppm (Figure 3a). The redox properties of complex **1** were investigated by cyclic voltammetry (CV) in phosphate buffer solution at pH 7. In phosphate buffer solution at pH 7, an irreversible reduction wave is observed at E$_{p,c}$ = − 0.20 V vs NHE and an irreversible oxidation wave at E$_{p,a}$ = 0.29 V vs NHE is observed

in the reverse scan (Figure 3b), both peaks are diffusion controlled (Figure 3c). These two peaks are assigned to the $Cu_3^{II}/Cu_2^{II}Cu_1^{I}$ reduction and oxidation, respectively.

Electrochemical studies

Electrochemical water oxidation using **1** was initially tested by CV in a one-compartment cell (Figure S2) in a phosphate-buffered solution at neutral pH (pH 7). A 0.5 mM solution of complex **1** displays an irreversible catalytic oxidation wave with $E_{cat/2}$ of 1.36 V vs NHE (Figure 4), which corresponds to an overpotential of ~550 mV.[72] After 15 consecutive scans at 20 mV/s with a glassy carbon working electrode, no deposition was observed by visual inspection. The carbon electrode was then rinsed with water and placed in a fresh electrolyte solution for subsequent analysis.[73] A slight increase in the current densities with respect to the background measurement was observed (Figure 4), suggesting that some deposition had occurred on the surface of the electrode. The changes observed in the CV waveform are most likely also due to copper deposition onto the GC electrode. However, the response was greatly diminished, indicating that the deposited material had minimal catalytic properties relative to the homogeneous species under these conditions.
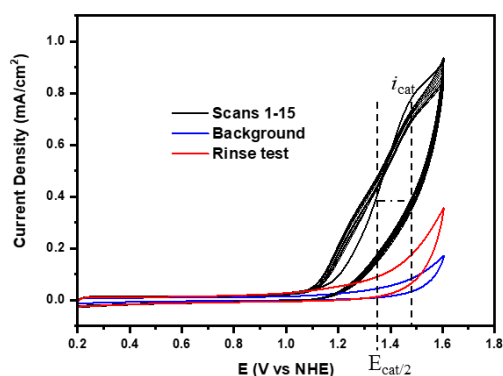

Figure 4. Consecutive cyclic voltammograms of 0.5 mM $[(DAM)Cu_3(\mu^3\text{-}O)][Cl]_4$ (**1**) at 20 mV/s (black) using a glassy carbon electrode at pH 7.0 0.1 M phosphate buffer solution. The CV from a rinse test after 15 scans is shown in red. The background CV in the absence of **1** is shown in blue.

CV studies of complex **1** in phosphate-buffered solutions were conducted at a wide range of pH values (2.1, 4.1, 8.1 and 11.5; Figure 5). Complex **1** appears to be an effective catalyst for electrocatalytic water oxidation at pH 7.0, 8.1 and 11.5 by CV (Figures 4, 5c and d). With the purpose of confirming the structural integrity of complex **1** at these pHs, ^1H NMR spectra of the complex was measured at pD 7.5, 8.9 and 11.9 in 0.1 M phosphate buffered D_2O (Figure S7). We found that the NMR spectra at these pHs is comparable to that of D_2O, indicating that the main structure of the complex is maintained under these conditions.
At pH 2.1, a new redox feature corresponding to the formation of copper (II) phosphate in solution appears at more reducing potentials ($E_{p,a} = 0.21$ V vs NHE; Figure 5a). At pH 8.1 and 11.5, a significant decrease in current density and changes in the waveform are observed through consecutive scans (Figures 5c and 5d), likely attributed to copper (II) phosphate or copper oxide formation, respectively, according to the potential-pH diagram and low solubility at these pHs.[74, 30] The variation in stability observed at the different pH values is also explained by the potential-pH diagram for a copper-phosphate-water system.[74] When a fluorine-doped tin oxide glass (FTO) electrode was employed as the working electrode at pH 8.1, instead of glassy carbon (GC), catalytic water oxidation is also observed, together with good reproducibility between consecutive scans (Figure 6). As a control experiment, copper (II) phosphate was prepared *in situ* by addition of $CuCl_2$ to phosphate buffer at pH 2.1 and 8.1. At pH 2.1, soluble copper phosphate is obtained which is inactive for water oxidation (Figure 7a). At pH 8.1, the addition of $CuCl_2$ to the phosphate buffer resulted in the precipitation of $Cu_3(PO_4)_2$ and the resulting suspension was found to be inactive for catalytic water oxidation (Figure 7b).[39] Importantly, none of these tests suggest that any of these possible decomposition products are responsible for the observed catalytic activity.
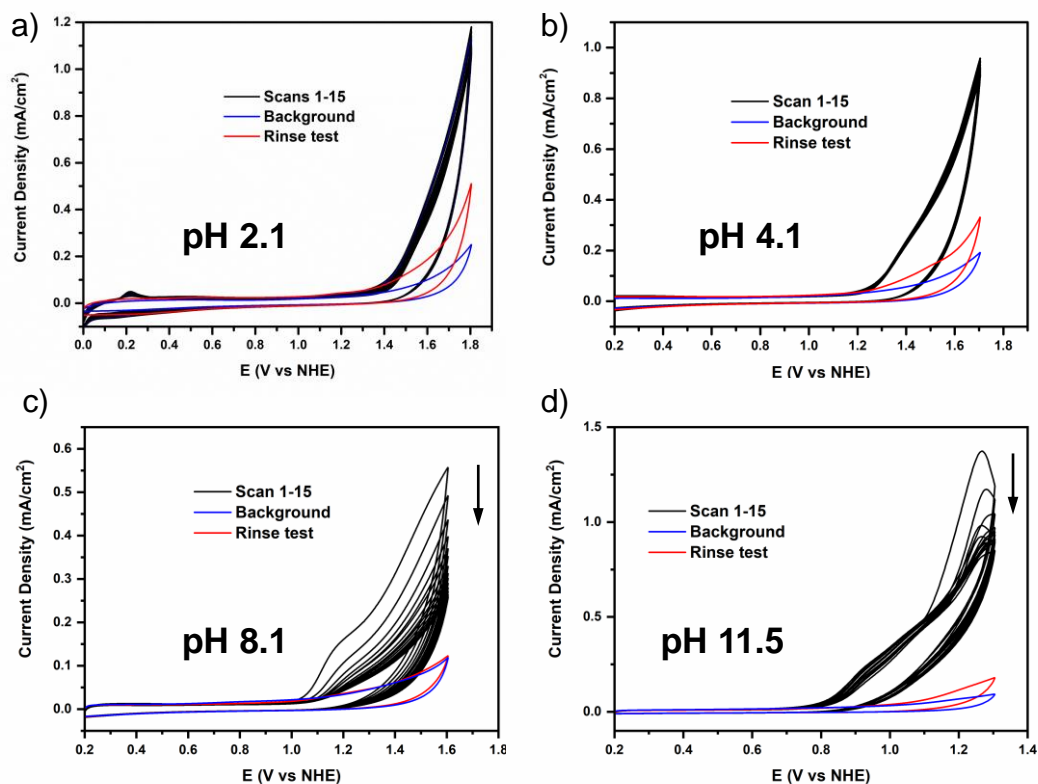
Figure 5. Cyclic voltammograms of [(DAM)Cu$_3$(μ^3-O)][Cl]$_4$ (**1**) at varying pHs: a) pH 2.1 b) pH 4.1 c) pH 8.1 d) pH 11.5. Conditions: 0.5 mM of **1**, GC electrode, scan rate = 30 mV/s, 0.1 M phosphate buffer solution.
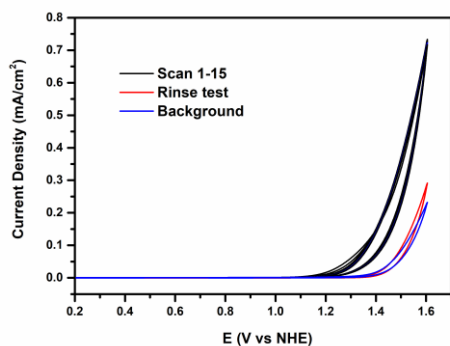
Figure 6. Cyclic voltammograms of [(DAM)Cu$_3$(μ^3-O)][Cl]$_4$ (**1**) at pH 8.1. Conditions: 0.5 mM of **1**, FTO electrode, scan rate = 30 mV/s, 0.1 M phosphate buffer solution.
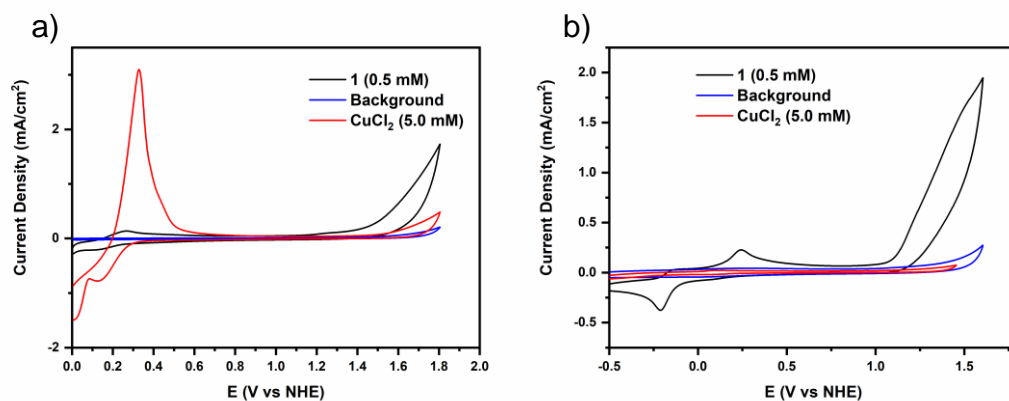
**Figure 7.** a) Cyclic voltammograms of in situ generated copper phosphate (red) and $[(DAM)Cu_3(\mu^3\text{-}O)][Cl]_4$ (**1**) (black) at pH 2.1. b) Cyclic voltammograms of in situ generated copper phosphate (red) and **1** (black) at pH 8.1. Conditions: GC electrode, 100 mV/s, 0.1 M phosphate buffer solution.

CV measurements confirmed that catalytic current densities, i_{cat}, increase with increasing concentration of **1** at pH 7 and, in a separate series of experiments, at pH 8.1 (Figures 8a and 8c). At both pH values, a linear relationship is observed from a plot of current density vs. concentration of **1** (Figures 8b and 8d). This indicates that the rate law for water oxidation catalyzed by **1** can be expressed by using a pseudo first-order rate constant. The peak current for the $Cu^{II/I}$ redox peaks are proportional to the square root of the scan rate at pH 7 (Figure S3b) and pH 8.1 (Figure S4b), which is indicative of diffusion-controlled redox processes.[75] Although a kinetically limited regime for the catalytic response could not be established in variable scan rate studies (Figures S3a and S4a), an upper bound for the first-order rate constant k_{cat} (or TOF) for the water oxidation reaction can be estimated from the catalytic current enhancement (i_{cat}/i_p) by applying equation 1:[76]

$$\frac{i_{cat}}{i_p} = 2.24 \frac{n_{cat}}{n_p^{3/2}} \sqrt{\frac{RTk_{cat}}{F\nu}} \qquad (1)$$

In this equation, ν is the scan rate, R is the universal gas constant, F is Faraday's constant, T is the absolute temperature, i_{cat} and i_p refer to the maximum current and the peak current of the $Cu^{II/I}$ redox couple, respectively. The term n_p is the number of electrons transferred at $E_{p,a} = 0.29$ V, which we *conservatively* estimated to be 1, and the number of electrons transferred in the catalytic process $n_{cat} = 4$ for water oxidation to dioxygen. We have used a corrected nc_{at} value which reflects the experimental efficiency for H_2O (see below). For pH 7.0 and 8.1, 45% of current generated O_2 in a 4-electron process while the rest is assumed to be H_2O_2 in a 2-electron process, therefore $n_{cat} = 2.9$ (0.45x4+0.55x2). The plot of i_{cat}/i_p versus $\nu^{-1/2}$ shows a linear relationship (Figure 9), the slope of which yields an estimated theoretical maximum TOF of 19.1 s^{-1} (Figure S3c) at pH 7 and of 57.7 s^{-1} (Figure S4c) at pH 8.1 at ~800 mV overpotential. These data are obtained using a GC working electrode, between each scan the GC electrode was cleaned with dilute HNO_3, polished and sonicated.
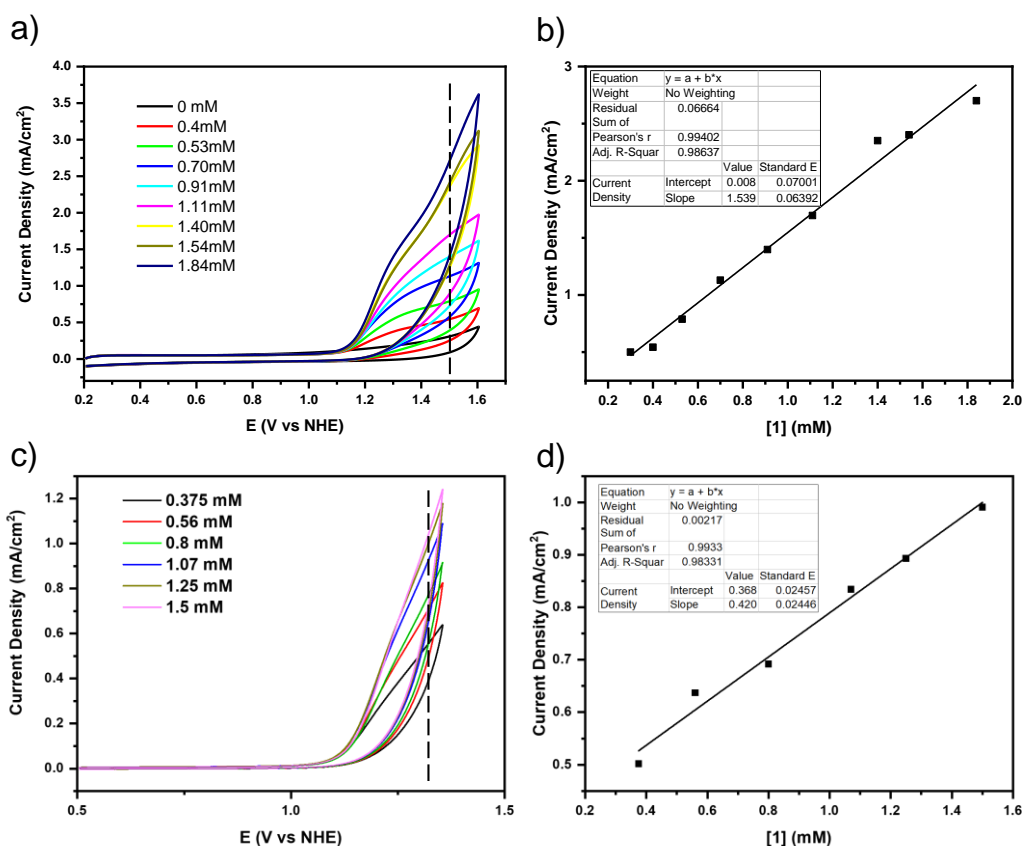


Figure 8. a) Concentration dependence by CV from 0 to 1.84 mM of $[(DAM)Cu_3(\mu^3\text{-}O)][Cl]_4$ (**1**) at pH 7. b) Plot of the current density respect to the concentration of **1** displaying linear concentration dependence of current density at 1.5 V at pH 7 phosphate buffer solution. c) Concentration dependence by CV from

0.38 to 1.5 mM of **1** at pH 8.1. d) Plot of the current density respect to the concentration of **1** displaying linear concentration dependence of current density at 1.3 V at pH 8.1. Conditions: GC electrode, 0.1 M phosphate buffer solution, scan rate = 100 mV/s.

The TOF values were also estimated from controlled potential electrolysis (CPE) data as described by Saveant and coworkers at pH 8.1 and 11.4 (see Supporting Information).[77] The TOF values were determined to be 1.9 s^{-1} at pH 8.1 and 99.4 s^{-1} at pH of 11.4.

The TOF values obtained for complex **1** are in the higher range for molecular copper catalysts at neutral pH (Table 1). The most active mononuclear copper WOCs at neutral pH are a copper(II) complex with a tetra-amidate macrocyclic ligand with a TOF of 140 s^{-1} at an overpotential of only 200 mV,[78] a copper(II) complex with a redox-active oxime ligand with TOF of 100 s^{-1} at an overpotential of 680 mV,[45] a copper(II) porphyrin, and a copper(II) complex with a tetradentate amine macrocycle both with TOF of 30 s^{-1} at an overpotential of 950 mV.[48, 46] For multinuclear copper WOCs the highest TOF are reported by Kiebler-Emmons and coworkers for the dinuclear complex, $[(Me_2TMPA-Cu_2)_2(\mu-OH)_2]^{2+}$, which was demonstrated to oxidize water with a TOF of 33 s^{-1} at pH 12.5 at ~1 V overpotential (Entry 1, Table 1) and for copper cubane complexes, $[(L_{Gly}-Cu)_4]$ and $[(L_{Glu}-Cu)_4]$ (L_{Gly} = 3-methoxy-salicylidene-glycine; L_{Glu} = 3-methoxy-salicylidene-glutamic acid), achieving TOF values at pH 12.5 of 267 s^{-1} at 1.2 V overpotential (entry 9, Table 1) and 105 s^{-1} at 1.1 V overpotential, respectively.[62, 42] However, these values are obtained in alkaline solutions at relatively high overpotentials. At neutral pH, dinuclear and multinuclear copper WOCs have sluggish rates. The two previously reported trinuclear copper WOCs, $[Cu_3(pda)_3(tBuPO_3)]\cdot 2(Et_3NH)$ and $[Cu_3(pda)_3(PhPO_3)]\cdot 2(Et_3NH)$ (pda = 2,6-pyridinedicarboxylic acid), have TOF of 0.82 and 0.58 s^{-1}, respectively, at pH 7 at ~800 mV overpotential (entry 5, Table 1).[59]

a)

b)
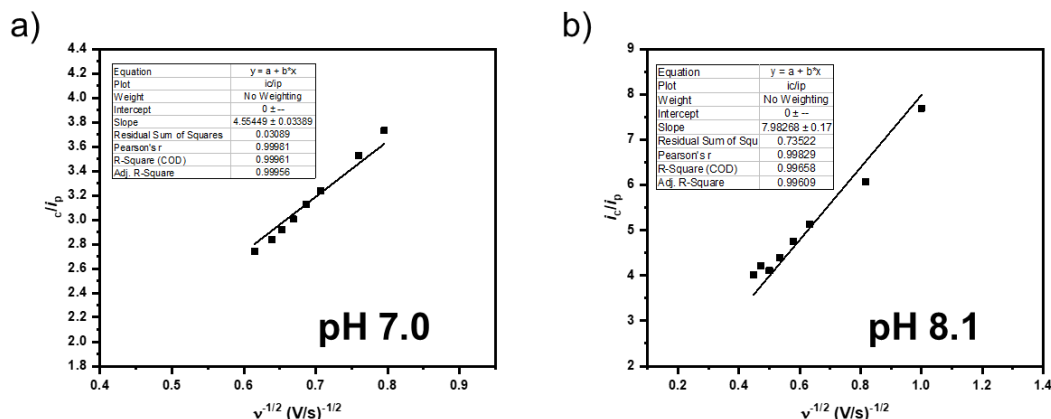
Figure 9. Plot of the ratio of the catalytic current at 1.6 V to the peak current for the Cu(II/I) couple vs. $v^{-1/2}$ with the intercept of the linear fit set at 0. Conditions: 0.5 mM of $[(DAM)Cu_3(\mu^3-O)][Cl]_4$ (**1**) in 0.1 M phosphate buffer solution at: a) pH 7 and b) pH 8.1.

Table 1. Selected examples of multinuclear copper water oxidation catalysts.

Entry	Catalyst	Concen. (mM)	pH	Electrolyte	η (mV)	TOF (s^{-1})	Reference
1	$[(Me_2TMPA-Cu_2)_2(\mu-OH)_2]^{2+}$	1.0	12.5	NaOH/NaOTf	720	33	37
2	$[Cu_2(BPMAN)(\mu-OH)]^{3+}$	1.0	7.0	PBS, 0.1 M	800	0.6	52
3	$[Cu_2(TPMAN)(\mu-OH)(H_2O)]^{3+}$	1.0	7.0	PBS, 0.1 M	780	0.78	54
4	$[Cu(oxpn)Cu(OH)_2]$	1.0	10.4	PBS, 0.25 M	640	6.7	56
5	$[Cu_3(pda)_3(PhPO_3)]\cdot 2(Et_3NH)$	0.5	7.0	NaOH/NaOAc	800	0.58	59
6	$[(DAM)Cu_3(\mu^3-O)][Cl]_4$ (**1**)	0.5	7.0	PBS, 0.1 M	800	19.1[(a)]	This Work
7	$[(DAM)Cu_3(\mu^3-O)][Cl]_4$ (**1**)	0.5	8.1	PBS, 0.1 M	800	3.6[(b)]/57.7[(a)]	This Work
8	$[(DAM)Cu_3(\mu^3-O)][Cl]_4$ (**1**)	0.5	11.4	PBS, 0.1 M	800	122.6[(b)]	This Work
9	$L_{Gly}-Cu_4O_4$	0.25	12.0	PBS, 0.2 M	620	267	62
10	$[Cu_4(H_2Lpa)_4]^{4+}$	0.2	12.5	NaOH/NaOAc	500	0.8	61
11	$[Cu_4(bpy)_4(\mu_2-OH)_2(\mu_3-OH)(H_2O)_2]^{2+}$	1.0	7.0	PBS, 0.1 M	730	-	60

Me$_2$TMPA = bis((6-methyl-2-pyridyl)methyl)(2-pyridylmethyl)-amine); BPMAN = 2,7-[bis(2-pyridylmethyl)aminomethyl]-1,8-naphthyridine; oxpn = N,N'-bis(3-aminopropyl) oxamido; pdaH$_2$ = 2, 6-pyridinedicarboxylic acid; DAM = dodecaaza macrotetracycle; L$_{gly}$ = 3-methoxy-salicylidene-glycine; H$_2$Lpa = 1,3-bis(6-hydroxy-2-pyridyl)-1H-pyrazole; bpy = 2,2'-bipyridine. (a) Determined by i_{cat}/i_p method (b) Determined from CPE data.

Using ^{1}H NMR spectroscopy, no evidence for deuterium exchange is observed with complex **1** in phosphate buffered D$_2$O solutions at pD 7; the same number of peaks are observed and no decrease in the intensity of any of the peaks is observed even after a week at room temperature (Figures S5 and S6). CVs of complex **1** in D$_2$O display a decrease in the catalytic current compared to CVs in H$_2$O under the same conditions (Figure 10). Although the catalytic response obtained in D$_2$O did not exhibit a clear current peak, we estimated a moderate KIE of 2.2(2) at 1.50 V by comparing the peak current observed for catalytic water oxidation in H$_2$O to the analogous experiment in D$_2$O (0.1 M phosphate buffer solution) according to equation 2, where the ratios of the apparent rate constants (k_{cat}) are proportional to the catalytic current (i_{cat}) ratio squared.[55] Note that the standard deviation is the result of three independent experiments. This KIE value is consistent with involvement of a proton in the rate determining step or preceding the rate determining step, resulting from cleavage of a water or phosphate O−H bond. The value is within the range (1.81-2.46) of those obtained for mononuclear and dinuclear copper complexes.[45, 54, 31, 34, 46, 48] This value is significantly smaller than the substantial KIE value of 20 obtained for a copper(II) dinuclear catalyst with a tris(pyrazolyl)amine type ligand.[42] It also differs from the lack of KIE (KIE = 1) observed for a copper (II) dinuclear complex with a naphthyridine ligand; in the proposed mechanism the O−O bond is formed by intramolecular coupling between a terminal copper hydroxo and a Cu$_2$(μ-O).[52, 53]

$$KIE = \frac{k_{cat,H_2O}}{k_{cat,D_2O}} = \left(\frac{i_{cat,H_2O}}{i_{cat,D_2O}}\right)^2 \qquad\qquad (2)$$
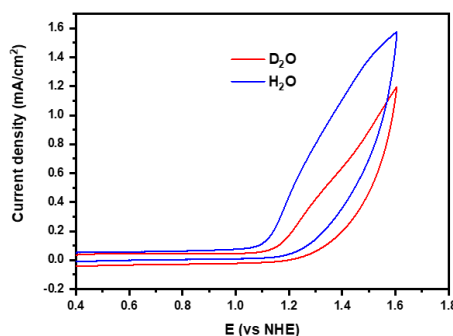
Figure 10. Comparison of electrocatalysis by [(DAM)Cu$_3$(μ^3-O)][Cl]$_4$ (**1**) in D$_2$O vs H$_2$O at 20 mV/s in 0.1 M phosphate buffer solution at pH 7 (blue) and 0.1 M deuterated phosphate buffer solution at pD 7 (red). The KIE was calculated to be 2.2(2) at 700 mV overpotential.

The influence of the electrolyte was tested by CV measurements in different buffers (Figure S7). Complex **1** was found to be unstable in borate buffer with the catalytic current decreasing significantly after just four scans. A current enhancement is observed in the phosphate buffer compared to the acetate buffer similar to other molecular water oxidation catalysts.[79-81]

In order to further understand the role of the buffer base, CV measurements at different phosphate base concentrations (0 to 0.2 M) were obtained while maintaining a constant ionic strength of the solution at 0.2 M with addition of NaNO$_3$ (Figure 11). The current density increases with the concentration of phosphate buffer in the range of 0 to 0.1 M. At high buffer concentrations ([phosphate buffer] > 0.1 M) an inhibition of the catalysis is observed,[79, 82] possibly due to the coordination of phosphate ligands to the metal center preventing the coordination of water. Assuming the main effect is the difference in proton acceptor ability and there is no inhibitory coordination effect of the nitrate anions, the enhancement in catalytic current with increasing phosphate concentration has previously been explained by the stronger proton acceptor ability of phosphate anions pK_a (H$_2$PO$_4^-$) = 7.2 respect to H$_2$O with pK_a (H$_3$O$^+$) = −1.74 and nitrate with pK_a (HNO$_3$) = −1.3, and the potential role of the phosphate in aiding the deprotonation of water during the rate-limiting O−O bond formation step.[80, 82, 31, 83, 58]
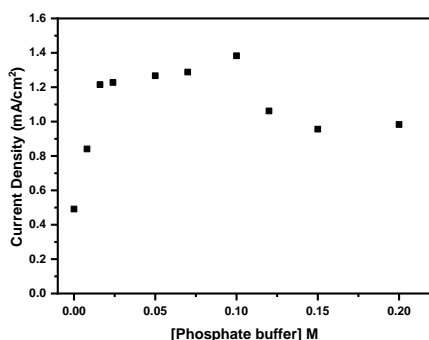
Figure 11. Plot of catalytic current density at 1.5 V respect to phosphate buffer concentration. Conditions: 0.5 mM of $[(DAM)Cu_3(\mu^3-O)][Cl]_4$ (**1**), pH = 7, scan rate = 100 mV/s. Ionic strength (I = 0.2 M) was maintained by addition of $NaNO_3$.

Dioxygen evolution was confirmed at pH 11.5 by CPE at 1.2 V on an FTO electrode with a surface area of 1 cm^2 employing 0.5 mM of **1** in 0.1 M phosphate buffer in a closed two-compartment cell with the cathode and anode separated by a Nafion^{TM} membrane (Figure S9). FTO was used as the working electrode due to its high surface area and high electrochemical stability at highly positive potentials with respect to GC (carbon oxidation to CO_2 can take place under harsh oxidizing conditions).[84, 85] CPE with a 0.5 mM solution of **1** displayed current densities between 1.5 and 2 mA/cm^2 with a gradual decrease in current over time (Figure 12a). After 3 h of CPE, the pH was found to be 10.9. We propose that a contributing factor to the observed decrease in current density during electrolysis can be attributed to the increasingly acidic pH. The dioxygen in the solution and headspace was measured using a calibrated Ocean Optics FOXY probe. Dioxygen production in the headspace at pH 11.5 occurs at a higher level than in control experiments without complex **1** (Figure 12b) with a Faradaic efficiency after 3 h of 81% and correcting for background dioxygen from cell leakage. After 3 h of CPE, no particle or film formation was detectable by scanning electron microscopy (SEM) of the FTO, and only small amounts of copper were detected by energy dispersive X-ray spectroscopy (EDX) on the FTO surface (Figure S11b). The FTO working electrode used for electrocatalytic water oxidation at pH 11.5 displayed no catalytic response in a fresh, catalyst free electrolyte solution at 1.2 V for 3 h (Figure 12a, blue trace).[73]

At a lower pH of 8.1, current densities of 0.5 mA/cm^2 were obtained by CPE at 1.37 V on an indium tin oxide (ITO) electrode with a surface area of 6.25 cm^2 in a 100 mL two-compartment bulk electrolysis cell (Figure S10) employing 0.5 mM of **1** (Figure 12c). Dioxygen was measured in the buffer solution using a calibrated Ocean Optics FOSPOR probe. Under these conditions and after correcting for background dioxygen from cell leakage, a Faradaic efficiency of 45% is obtained after 40 min of CPE. The ITO working electrode used for electrocatalytic water oxidation at pH 8.1 at 1.37 V for 40 min, displayed a significantly reduced catalytic response in a fresh, catalyst free electrolyte solution (Figure 12c, blue trace).[73] The activity observed in the first three minutes of the rinse test is likely due to physisorption of complex **1** onto the FTO electrode. After 40 min of CPE, no particle or film formation was detectable by SEM, and trace amounts of copper were detected by EDX over the surface of the ITO (Figure S11d). These data are consistent with a homogeneous process under these conditions. UV-Vis spectra before and after the electrolysis at both pH values (11.5 and 8.1) show a decrease in absorbance after the catalysis (Figure S12). The relatively low Faradaic efficiencies, coupled with the change in solution composition, are an indication of potential degradation of **1** to non-catalytic species under the oxidative conditions of catalysis.

10
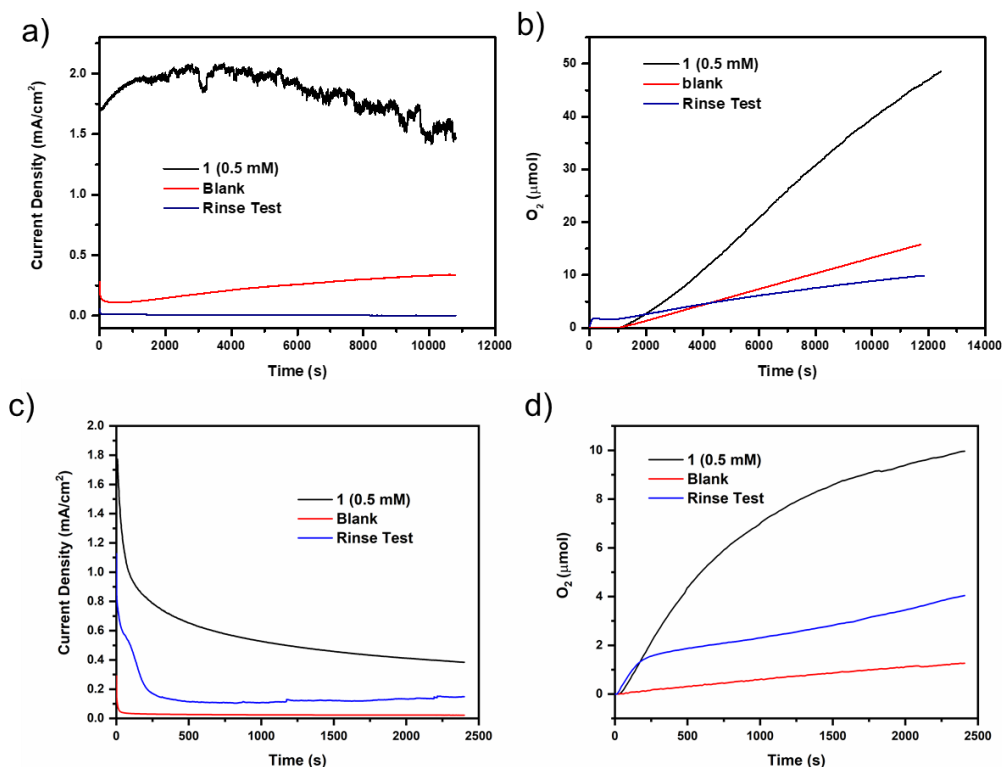
Figure 12. a) Current density during controlled potential electrolysis (CPE) with **1** (0.5 mM), without catalyst and during a rinse test at pH 11.5 at 1.2 V vs. NHE. b) Dioxygen concentration in the headspace during CPE with **1** (0.5 mM; black trace), without catalyst (red trace) and during a rinse test (blue trace) at pH 11.5 at 1.2 V vs. NHE. c) Current density during CPE with **1** (0.5 mM; black trace), without catalyst (red trace) and during a rinse test (blue trace) at pH 8.1 at 1.37 V vs. NHE. d) Dioxygen concentration in the solution during CPE with **1** (0.5 mM; black trace) and without catalyst (red trace) at pH 8.1 at 1.37 V vs. NHE.

Due to the moderate Faradic efficiencies obtained, experiments were performed to investigate water oxidation selectivity with a rotating ring (Pt)-disk (GC) electrode (RRDE). At both pH 11.2 and 8.1, no anodic current of H_2O_2 oxidation could be detected at the Pt ring electrode indicating the likely absence of H_2O_2 providing evidence for selective oxidation of water to dioxygen (Figure 13).
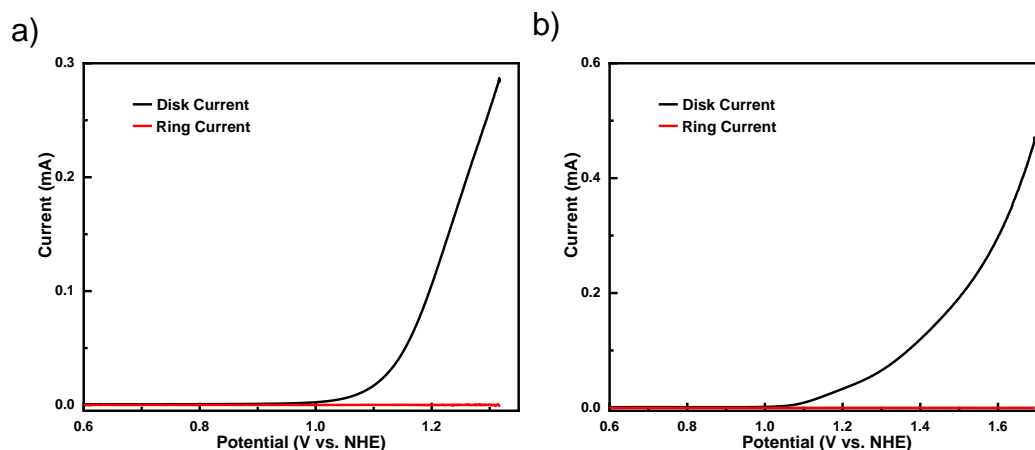
Figure 13. a) Rotating ring (Pt)-disk (GC) electrode (RRDE) Analysis of 0.5 mM $[(DAM)Cu_3(\mu^3\text{-}O)][Cl]_4$ (**1**) in pH 11.2 0.1 M phosphate buffer solution. The potential of the ring electrode is maintained at 0.76 V vs. NHE. Rotation rate is 1600 rpm, and the scan rate is 10 mV/s. b) Rotating ring (Pt)-disk (GC) electrode (RRDE) Analysis of 0.5 mM **1** in pH 8.1 0.1 M phosphate buffer solution. The potential of the ring electrode is maintained at 0.85 V vs. NHE. Rotation rate is 1600 rpm, and the scan rate is 10 mV/s.

EPR studies

To further investigate complex **1** under catalytic conditions and identify potential decomposition of the complex during electrolysis, EPR spectra were recorded of a 50 mM solution of **1** in 0.1 M phosphate buffer solution at pH 7. Higher concentrations of **1**, relative to electrochemical experiments, were used due to the low EPR signal from the complex. The frozen solution EPR spectrum of the pristine reaction solution is shown in Figure 14 (black spectrum). Such a solution was then used in an electrochemical two-electrode cell, applying a potential of 2 V between a glassy carbon and a platinum electrode. While operating, the cell was freeze-quenched in liquid nitrogen. In this frozen state the potential was switched off and the cell was disassembled. A piece of the frozen solution, which was attached to the glassy carbon, was inserted into a precooled EPR tube and directly transferred to the EPR resonator in a cryostat at 5 K (Figure 14, red spectrum). After the measurement, the sample was warmed to room temperature outside the cryostat and reinserted after 30 minutes to record another EPR spectrum at 5 K (Figure 14, blue spectrum).

The EPR spectra consist of two contributions, one originating from complex **1** and another from dioxygen in the sample. At X-band, dioxygen induces a characteristic signal at ~1200 mT, which can be used as a fingerprint for the presence and concentration changes of dioxygen.[86] It can easily be distinguished from the EPR spectrum of complex **1,** which had previously been reported by Solomon and Yoon.[71] The latter consists of two lines, one at an effective g factor of $g_{eff} = 2.1$ and another at $g_{eff} = 4.3$, which is characteristic for a high spin complex. The EPR spectrum contribution of complex **1** in buffer solution differs from the EPR spectrum of the solid powder and cannot be fitted accurately with the published parameters.[71] The interaction of complex **1** with the electrolyte seems to induce a significant change in the electronic structure, and a fitting based on one frequency band would be debatable.

When comparing the EPR spectrum of the fresh reaction solution with the freeze-quenched spectrum of the running cell, changes can be identified.[87] The increased amount of dissolved dioxygen caused by electrolysis is visible, providing additional confirmation of the catalytic formation of dioxygen. After thawing and refreezing the dioxygen peak decreases again, indicating dioxygen concentration equilibration in a previously oversaturated solution, which demonstrates the successful freeze quenching of the solution during the OER. Furthermore, the EPR peak at $g_{eff} = 2.1$ increases and shifts to a slightly lower g_{eff}. The large line width prevents an exact assignment of this effect. Since the $g_{eff} = 4.3$ peak is hardly affected, it may tentatively be assigned to a reduction of anisotropies that initially show a broader distribution. However, this needs to be investigated in more detail in future work. On the other hand, it can be excluded that this signal belongs to a mononuclear Cu(II) complex with spin $S = \frac{1}{2}$ that may be formed due to degradation of complex **1**, because there is no observable hyperfine structure or typical anisotropic features that are very characteristic for such spin systems.[88] The change in the spectrum is likely caused by a complex that still maintains a copper trinuclear core. Warming the freeze-quenched sample induces further change in the complex **1** EPR spectrum, suggesting that freeze quenching could successfully capture a transient state and that a stable odd-electron intermediate from the catalytic cycle exists.
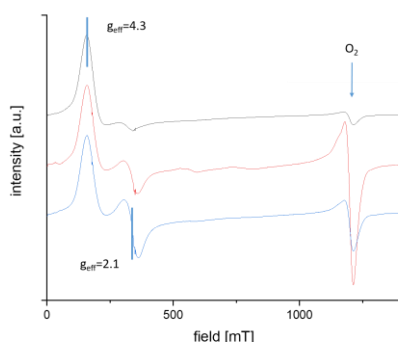
Figure 14. X-band c.w.-EPR spectrum (9.734 GHz microwave frequency) of a 50 mM reaction solution of [(DAM)Cu₃(μ³-O)][Cl]₄ (**1**) in 0.1 M phosphate buffer solution at pH 7 at 5 K. Pristine reaction solution under air (black), freeze-quenched reaction solution of a running electrolysis (red), and the same sample recorded post-test after standing 30 min at room temperature (blue).

DFT calculations
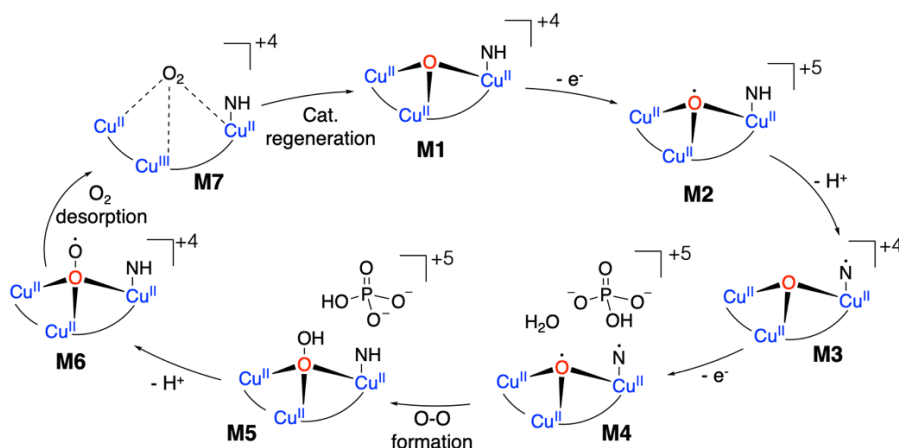
Scheme 3. Mechanism for the oxygen evolution reaction on $[(DAM)Cu_3(\mu^3\text{-}O)][Cl]_4$ (**1** or **M1**).

Density Functional Theory (DFT) was used to probe the reaction mechanism. We have previously used this methodology to determine the reaction mechanism and rate constants for the OER on several electrocatalysts: IrO_2,[89] Fe doped $NiOOH$,[90] Ir doped $(Ni,Co)OOH$,[91] and Co-doped TiO_2.[92] The results of the calculations are overviewed in Schemes 3, 4 and 5.

The initial unactivated complex, trinuclear Cu(II) complex **1** is labeled **M1** (Scheme 3), which has 3 Cu^{II} sites bridged by a single O atom, leading to 3 unpaired spins to give an overall S = 3/2 quartet state. The DFT-optimized structure is compared with the crystal structure in Figure 2. The predicted minimized bond distances are Cu–O = 1.96 Å compared to ~1.90 Å in the experimental crystal structure (Figure 2). The DFT predicted Cu–O–Cu angle is 107.8 ° compared to 111.5 to 111.9 ° from the experimental crystal structure. The DFT calculations were performed using the high-spin state, S = 3/2. From the EPR data we can exclude the formation of a stable S = 1/2 state, as we would expect a room temperature spectrum and no g_{eff} = 4.3 peak. As the frozen state of the system is a high-spin state this state is likely lower in energy. However, we cannot discard a mixture of an S = 1/2 state and S = 3/2 state.

Removing an electron from **M1** gives **M2** with a total of four unpaired spins. We calculated the high-spin S = 2 state with DFT. We again anticipate the possibility of one low-lying singlet state and one low-lying triplet state, but these cannot be reliably obtained from DFT. For **M2**, all Cu–O distances remain ~1.96 Å. The only notable change in **M2**'s structure is that the axial Cu-N distances increase from 2.25 Å to 2.4 Å, indicating decreased donor-acceptor interactions (Figure 15). We calculate the ionization potential from **M1** to **M2** to be 5.44 eV (125.4 kcal/mol) in implicit phosphate solvent. Taking the reference for NHE as 4.42 eV, this corresponds to 1.02 V_{NHE} or 1.69 V_{RHE} at pH = 11. This is in reasonable agreement with our experimental observation of 1.2 V vs. NHE at pH = 11.5. At 1.2 V vs. NHE, conversion of **M1** to **M2** is downhill 4.2 kcal/mol, as opposed to uphill 125.4 kcal/mol in the absence of a potential.
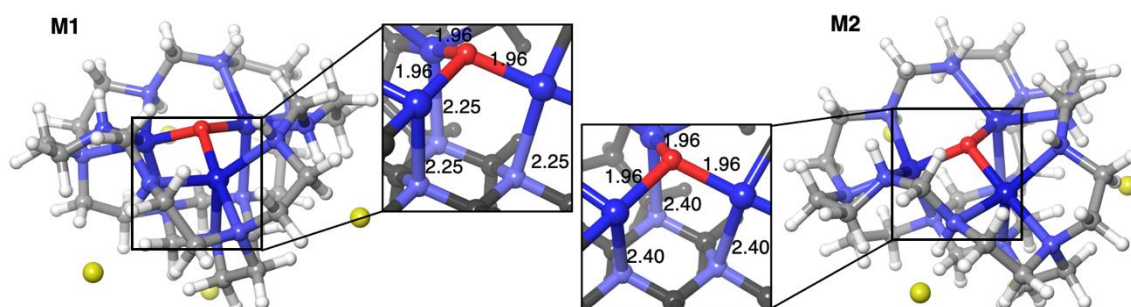
Figure 15. DFT-optimized **M1** (left) and **M2** (right) with closeups on the active sites (distances are in Å). The two structures are nearly identical with the 3 Cu-O distances remaining 1.96 Å, although the axial Cu-N distances increase from 2.25 Å in **M1** to 2.4 Å in **M2**.

We predicted oxidation and reduction reactions of **M1** (Figure S13) using DFT (including van der Waals corrections with PBF implicit solvent and using the vibrational frequencies to convert QM results to free energy activation energies at reaction temperature). Since a second oxidation of **M1** was found to be highly unfavorable, we instead considered the deprotonation of a secondary amine ligand. This renders a second oxidation (to **M4**) feasible. Deprotonation of **M2** to form water (**M2** + OH^- → **M3** + H_2O) occurs

13

at a N-bonded to Cu(III). We calculate the structure assuming high spin with four unpaired electrons (i.e. the $S = 2$ quintet state). The most energetic unpaired spin on the N should spin pair with the Cu spin to form an $S = 1$ state. DFT predicts this open shell triplet to be 0.9 kcal/mol lower than the $S = 2$ quintet, such that the triplet and quintet are nearly degenerate energetically. Deprotonation of N decreases the Cu–N bond distance to 2.15 Å from 2.23 Å in **M2**. The formation of **M3** (Scheme 4) is calculated to be 4.0 kcal/mol downhill relative to **M2** and 121.4 kcal/mol uphill relative to **M1** (ignoring the applied potential).

We predict that **M3** is converted to **M4** upon another single-electron oxidation. The reaction of **M4** in association with water and phosphate leads to O–O bond formation (transition state **M4TS** discussed below). Geometry optimization of the **M4-**phosphatewater complex leads to three hydrogen bonds. The water forms two hydrogen bonds: one to the copper oxo and one to the phosphate. The phosphate makes one hydrogen bond to the water. Note that for O–O bond formation, the hydrogen bond between the water and the copper oxo must be broken.

The product of O–O bond formation is **M5** with a bridging hydroperoxide ligand, which is 8.3 kcal/mol below **M4**. The subsequent steps for OER are: the OOH ligand is deprotonated to give **M6**. Triplet O_2 then desorbs from the complex to yield **M7**. Following liberation of dioxygen from **M7**, **M1** can be regenerated by reaction with an incoming water molecule to form the μ-OH copper species. Subsequent deprotonation of the μ-OH by a nearby phosphate or hydroxy group yields **M1**.[52]
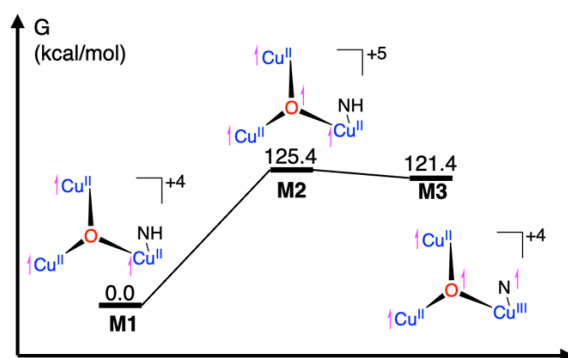
Scheme 4. DFT free energy profile at 298 K for the preparation of **M1** towards water oxidation. Each state has 4 Cl⁻ counterions to balance charge and to reduce solvation energy error for charged species.
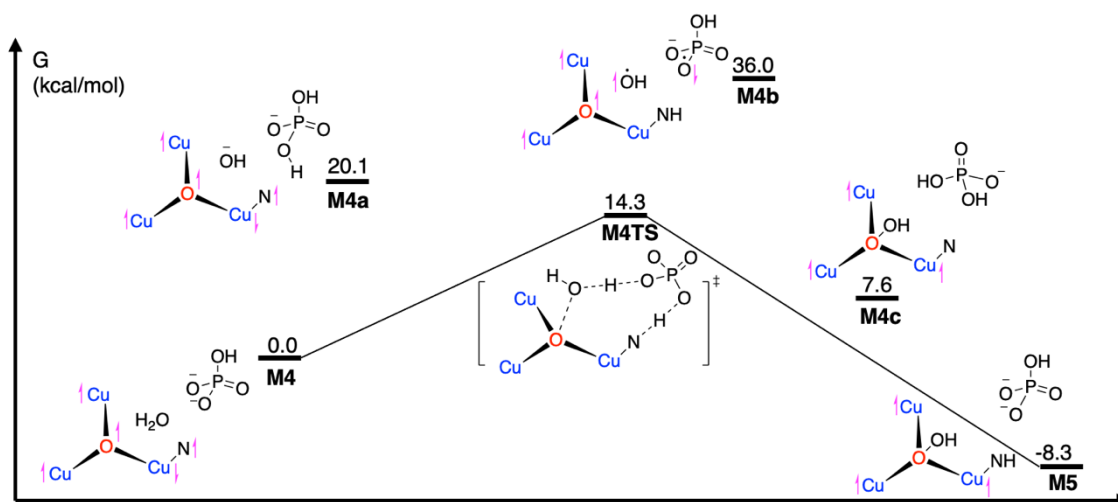
Scheme 5. DFT free energy profile at 298 K for the oxygen-oxygen coupling mechanism. 3 Cl⁻ counterions are included in the calculation for charge balance and to reduce solvation energy error for charged species.

Our DFT calculations find that O–O bond formation is enabled by a second-sphere phosphate (Scheme 5) in a transition state that involves one H_2O and one $O=P(O)_2OH$. In the calculated transition state (**M4TS**), an explicit singly-protonated phosphate is within van-der-Waals distance of the N with the unpaired spin, while a water molecule is near the O radical site and the phosphate as seen in Figure 16. We calculate a concerted process in which: (a) an O–O bond is formed between the copper oxo and water, (b) water

transfers a proton to the phosphate, and (c) the phosphate transfers a proton to the deprotonated nitrogen. Thus, phosphate serves as a proton shuttle and the pendent N is important for the critical O−O bond forming step. Calculations without an explicit phosphate result in a barrier of 32 kcal/mol, which is too high to corroborate the experimentally observed reaction rate.

The 9-membered transition state (**M4TS**) for the rate-limiting O−O bond formation, leads to a 14.3 kcal/mol barrier above the **M4** state with an imaginary frequency of -1054 cm^{-1}. At pH 8.1 and 11.4, the experimentally observed TOFs for water oxidation are 1.9 and 99 s^{-1}, respectively. These experimental TOFs correspond to free energy barriers of 17.1 and 14.7 kcal/mol, in excellent agreement with the 14.3 kcal/mol barrier predicted by DFT. Again, the product state **M5** with new O−O and N−H bonds is 8.3 kcal/mol downhill from the reactant **M4**, confirming the reaction is favorable.

However, the O−O bond formation could also occur through a stepwise mechanism in which O−O bonding, O−H bond dissociation, and N−H bond dissociation do not occur simultaneously. We predict free energies of several possible intermediates to probe for potential stepwise mechanism (Scheme 5). One possible route is two concerted hydrogen transfers (one from water to the phosphate and one from phosphate to the nitrogen) followed by O−O coupling. The intermediate state between these two steps (**M4b**) is 36.0 kcal/mol above the reactant state, which is well above our concerted transition state **M4TS**, making this two-step pathway unfavorable. Another route for water oxidation is proton transfer from the water to the phosphate (making the phosphate doubly protonated), followed by concerted O−O bond formation and phosphate to nitrogen proton transfer. This path goes through intermediate **M4a**, which is 20.1 kcal/mol higher than the reactant. Again, this intermediate is higher in energy than **M4TS**, making it unfavorable. Thus we consider that this two-step mechanism is not responsible for O−O bond formation. Finally, we can envisage a path where concerted water to phosphate proton transfer and O−O bond formation occur, followed by phosphate to nitrogen proton transfer. This intermediate (**M4c**) is 7.6 kcal/mol above the starting state. While this reactant is lower in energy than the other alternative intermediates, it is 15.9 kcal/mol above **M5** with the O−O already formed, suggesting that the preceding O−O bond forming transition state would be significantly higher than **M4TS**. Thus the pathway through **M4c** is not favorable. These alternative intermediates are too high in free energy to have transition states lower in energy than **M4TS**, indicating that any route through these intermediates is less favorable than the concerted pathway with its free energy barrier of 14.3 kcal/mol in basic conditions.
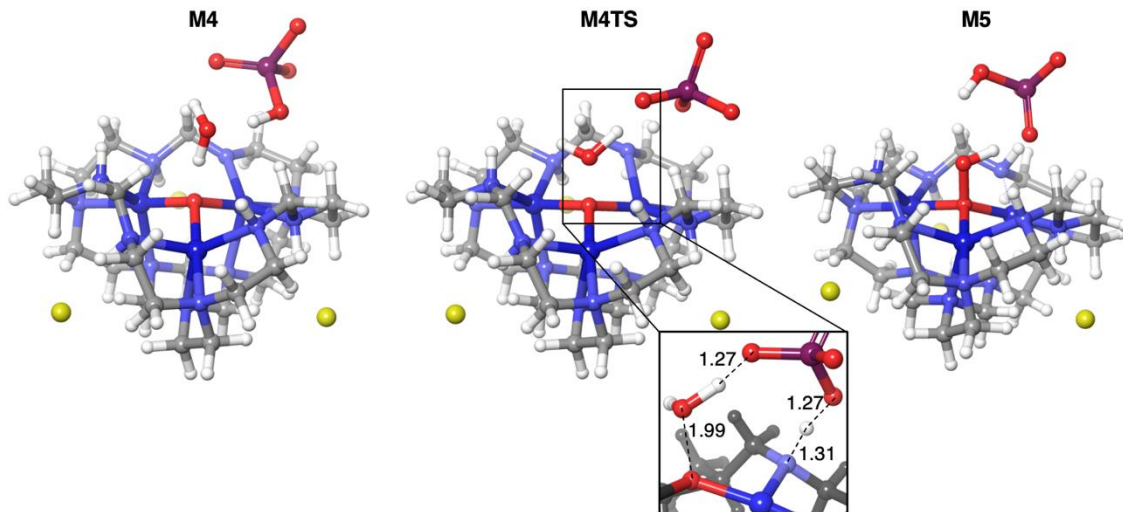
Figure 16. DFT-optimized reactant (**M4**), transition state (**M4TS**), and product (**M6**) geometries for the O−O bond formation step.

Summary and Conclusions

In summary, our results demonstrate that [(DAM)Cu$_3$(μ^3-O)][Cl]$_4$ (**1**) is a catalyst precursor for selective electrochemical water oxidation to form dioxygen in phosphate buffered solutions at pH 7.0, 8.1 and 11.5. Measurements during controlled potential electrolysis verify the formation of dioxygen, while RRDE experiments confirm the selectivity to dioxygen. Control experiments are consistent with a homogeneous molecular catalyst as the active species. The secondary amine groups on the dodecaaza macrotetracycle ligand can provide hydrogen bonded networks, which aid in aqueous solubilization and stability. Moreover, DFT calculations indicate that the -NH- groups of the ligand are important in providing a pathway for proton movement in the vicinity of the copper center. Additionally, both experimental and

computational studies show that the choice of buffer base plays a critical role in molecular electrocatalytic water oxidation acting as a proton acceptor. This work highlights the importance of ligand design and the potential role of intramolecular proton relays in electrochemical water oxidation.

Experimental Section

General Methods. All reagents and solvents were purchased from commercial sources and used without further purification unless stated otherwise. Deionized water was obtained from a Millipore Autopure system (18.2 MΩ, Millipore Ltd., USA). UV-Vis absorption spectra were recorded using a Cary 60 UV-Vis Spectrophotometer. Scanning electron microscope (SEM) images and energy dispersive X-ray analysis (EDX) data were obtained at FEI Quanta 650. ^{1}H NMR spectra are referenced to tetramethylsilane (TMS) using residual proton signals (^{1}H NMR) of deuterated solvents and were recorded using a Bruker AV800 spectrometer. Deuterated solvents were used as received from a commercial source. Continuous wave (c.w.) X-band EPR measurements were performed on an ElexSys 560 spectrometer, equipped with an ER 4118X-MD5 Resonator and an Oxford Instruments cryostat. Microwave power was set to 0.75 mW, the field modulation frequency was 100 kHz, and the modulation amplitude was 4G. Infrared spectra were obtained using diffuse reflectance infrared Fourier-transform spectroscopy (DRIFTS) with Nicolet iS 50 FT-IR (Thermo Scientific, USA) equipped with a DiffusIR™ diffuse reflectance cell (Pike Technologies). Elemental analyses were performed by Midwest Microlab, Indianapolis, IN, or the UVA Chemistry Department, Charlottesville, VA.

Synthesis of [(DAM)Cu₃(μ₃-O)][Cl]₄ (1). The reaction was carried out under an atmosphere of dinitrogen inside a glovebox using a modification of a published procedure.[68] To a dry methanol solution (100 mL) of $CuCl_2$ anhydrate (1.38 g, 10.3 mmol) were added tris(2-aminoethyl)amine (3.14 g, 20.6 mmol) and paraformaldehyde (3.0 g, 100 mmol). The dark blue solution was heated at reflux for 20 hours until green precipitate was observed. The reaction mixture was filtered through a fine porosity frit, and the solid was washed with dry ethanol (20 mL) and dried in vacuo. The volume of filtrate was reduced to half in vacuo, and then the concentrated filtrate was heated to reflux. After 10 hours, green precipitate formed again. The green solid was collected by filtration out and washed with dry ethanol (20 mL) and dried in vacuo. Isolated yield of two filtrations = 67.3%. ^{1}H NMR (800 MHz, D_2O, 25 °C): δ 433.5 (s, 1H), 258.6 (s, 1H), 231.7 (s, 1H), 205.5 (s, 1H), 189.9 (s, 1H), 135.0 (s, 1H), 68.7 (s, 1H), 54.8 (s, 1H), 38.3 (s, 1H), 35.3 (s, 1H), 34.1 (s, 1H), 9.1 (s, 1H), 8.5 (s, 2H), 4.3 (s, 1H), -0.6 (s, 1H). IR (ν_{NH}): 3240 cm^{-1}. μ_{eff} (Evans, D_2O, 25 ºC) = 3.2 μ_B. Anal. Calcd for $C_{24}H_{54}N_{12}OCl_4Cu$: C, 33.55; H, 6.34; N, 19.56. Found: C, 32.99; H, 6.54; N, 19.16.

Electrochemistry. Unless otherwise noted, electrochemistry was performed using a CH Instruments CHI630E potentiostat. All electrochemical experiments were performed at room temperature. Glassy Carbon (GC), 1 cm² fluorine-doped tin oxide glass (FTO) or 6.25 cm² indium tin oxide (ITO) was used as working electrode, Ag/AgCl (3 M NaCl) as reference electrode and Pt wire as counter electrode. All potentials are reported versus the normal hydrogen electrode (NHE) by adding 0.205 V to the measured potential. GC working electrodes were polished for 10 minutes with a 0.05 μm Al_2O_3 slurry, sonicated for 10 min in ultrapure water, and then rinsed prior to each experiment. FTO electrodes were sonicated in ultrapure water for 10 min and rinsed before each experiment. Solutions were purged with dinitrogen for 10 min, and a stream of dinitrogen was maintained over solutions for the duration of the experiments. Cyclic voltammetry (CV) experiments were performed with a three-electrode system in a one compartment electrochemical cell. The reference and counter were as described above. In normal CV experiments, a 3.00 mm (0.0707 cm²) geometric-diameter glassy carbon (GC) working electrode (BASi) was used.

Rotating ring (Pt)-disk (GC) electrode (RRDE) analysis. H_2O_2 was detected by electrochemical measurements using rotating ring (Pt)-disk (GC) electrode (RRDE) analysis. A Pine Research Rotating Ring Disk Electrode was employed with an electrode composed of a GC disk and a Pt ring electrode, with a collection efficiency of 37%, a ring-disk gap of 320 μm and the following diameters: 5.61 mm disk outer, 7.92 mm ring outer and 6.25 mm ring inner. The solution is placed in a one-compartment cell with a the RRDE, reference (Ag/AgCl and HgO) and counter electrode (Pt) and nitrogen flow tubes, all of them fitting tightly. The electrodes were connected to a Biological potential station (Model VMP3) for electrochemical measurements. Before each experiment, the solution was purged with nitrogen during 30 minutes, and then a nitrogen atmosphere was maintained during the measurement. Electrochemical studies of complex **1** were conducted in 0.1 M pH 11.2 phosphate buffer (0.1 M) using linear sweep voltammetry (LSV) of the disk electrode with a scan rate of 10 mV/s.

Turnover frequency (TOF). Turnover frequency (TOF) was calculated from the i_{cat}/i_p ratio as described in equation 1.[76] The peak current for the oxidation $Cu_3^{II}/Cu_2^{II}Cu_1^{I}$ peak at $E_{p,a} = 0.29$ (i_p) was proportional to the square root of scan rate as required by the Randles-Sevcik equation. In order to reach steady-state conditions, CV was measured using high scan rates (1-8 V/s). The measured maximum catalytic current (i_{cat}) varied linearly with the concentration of catalyst.

$n_p = 1$ and is the number of electrons transferred in non-catalytic process ($Cu_3^{II}/Cu_2^{II}Cu_1^{I}$ peak)

n_{cat} reflects the experimental efficiency for H_2O. For pH 7.0 and 8.1, 45% of current generated O_2 in a 4-electron process while the rest is assumed to be H_2O_2 in a 2-electron process, therefore $n_{cat} = 2.9$ (45%x4+55%x2)

$$\frac{i_{cat}}{i_p} = 2.24 \frac{n_{cat}}{n_p^{3/2}} \sqrt{\frac{RTk_{cat}}{Fv}} \qquad (1)$$

The TOF values were also calculated from CPE data as described by Saveant and coworkers (see supporting information for a more detailed description).[77]

Controlled Potential Electrolysis (CPE). Controlled potential electrolysis experiments were performed in a either glass two-compartment cell separated by **Nafion**[TM] membrane or a 100 mL 2-compartment bulk electrolysis cell separated by a buffer saturated glass membrane and electrodes sealed with Dow Corning high vacuum grease. The **Nafion**[TM] membrane (Nafion[TM]-212, 50 μm thick, Sigma) was cut in square 4 x 4 cm pieces, and conditioned by sonicating in H_2O_2 (10% in H_2O), then in H_2SO_4 (0.5 M) then in H_2O for 30 min (2x) with thorough rinsing in water between each step, then stored in ultrapure water and superficially dried before use. For the two-compartment cell separated by Nafion[TM] membrane, one side of the cell contained a 1 cm^2 FTO working electrode and Ag/AgCl (3 M NaCl) reference electrode. While for the 100 mL 2-compartment bulk electrolysis cell 6.25 cm^2 ITO is used as the working electrode. The other side contained a platinum wire counter electrode. Before starting the experiment, the side of the cell with the working electrode was purged with dinitrogen for 30-60 minutes. The cell was sealed and dioxygen concentration was measured before and during the electrolysis. During the experiment, the solutions in the compartments with the working electrode was vigorously stirred. The produced dioxygen was quantified in the headspace or solution using an Ocean Optics FOSPOR probe (Model NeoFox); the dioxygen probe was calibrated using a two-point calibration procedure with NeoFox Viewer software. The results of the CPE with complex **1** was compared with a blank experiment in the same conditions but in the absence of catalyst. The Faradaic efficiency was determined according to the total charge passed during the CPE and the total amount of generated dioxygen by taking into account that water oxidation is a 4 oxidations process. After each CPE experiment, the working electrodes were rinsed with water and placed in fresh buffer solution to perform a CPE experiment in the absence of catalyst (rinse test).

X-ray Diffraction of [(DAM)Cu₃(μ³-O)][Cl]₄ (1). Crystals of **1** were grown by slow evaporation of an acetonitrile/water (2:1) solution. Single-crystal X-ray diffraction data were collected on a Bruker Kappa APEXII Duo diffractometer running the APEX3 software suite using the Mo Kα fine-focus sealed tube ($\lambda = 0.71073$ Å). The structure was solved and refined using the Bruker SHELXTL software package within APEX3 and OLEX2, using the space group P-1, with Z = 2 for the formula unit, $C_{24}H_{54}Cl_{3.56}Cu_3N_{12}O$.[93, 94] Non-hydrogen atoms were refined anisotropically. Hydrogen atoms were placed in geometrically calculated positions with $U_{iso} = 1.2U_{equiv}$ of the parent atom. The relative occupancies of the disordered atoms were freely refined, and no constraints or restraints were used on the bond lengths or anisotropic displacement parameters of the disordered atoms. The solvent and one chloride anion were severely disordered and could not be successfully modeled with or without restraints. Thus, the structure factors were modified using the PLATON SQUEEZE technique, in order to produce a solvate-free structure factor set.[95] PLATON reported a total electron density of 135 e⁻ and total solvent accessible volume of 325 Å^3. The final anisotropic full-matrix least-squares refinement on F^2 with 571 variables converged at R1 = 4.06%, for the observed data and wR2 = 10.18% for all data. The goodness-of-fit was 1.024. The largest peak in the final difference electron density synthesis was 1.254 e⁻/Å^3 and the largest hole was -1.811 e⁻/Å^3 with an RMS deviation of 0.098 e⁻/Å^3. On the basis of the final model, the calculated density was 1.430 g/cm^3 and F(000), 875 e⁻. The crystal data are summarized in Table S1.

Computational Methods. All quantum chemical calculations were carried out using the Jaguar software version 10.9 by Schrodinger Inc.[96] Structure optimizations were performed in implicit solvent using the B3LYP[97] flavor of DFT including the Grimme-Becke-Johnson D3 correction for London dispersion (van der Waals attraction).[98] Organic elements were described using the triple-zeta 6-311G**++ basis set[99, 100] while Cu was treated using the Los Alamos small-core (18 explicit electrons) effective core potential, LACV3P**++.[101, 102] B3LYP-D3 structure optimizations were followed by single-point energy calculations using the M06-2X flavor of DFT[103] with the D3 correction and ultra-fine DFT grids.

To predict thermochemical properties at 298 K, we calculated the vibrational frequencies at the M06-2X-D3 level to obtain zero-point energies, enthalpies, and entropies. These frequency calculations were also used to confirm that there are no negative eigenvalues of the Hessian for minima and only a single negative eigenvalue for transition states. For reactions in which a single molecule leads to two molecules in the product, the above calculation assumes that the second molecule has 6 free translation and rotation modes, whereas in our experiments it will lead to 6 hindered vibrational modes. We correct for the gas-phase entropy by reducing entropic contributions of these 6 degrees of freedom by 50%.

Both the B3LYP-D3 geometry minimizations and M06-2X-D3 single point calculations included implicit solvent at the PBF level implemented in Jaguar.[104] PBF is based on the solvent accessible surface using an effective solvent radius and dielectric constant. To capture the solvent environment of 0.1 M phosphate-buffered solution, we used a probe radius of 3.0 Å and a dielectric constant of $\varepsilon = 78.3$ from Elmore.[105]

■ **ASSOCIATED CONTENT**

Supporting Information

The Supporting Information is available free of charge on the ACS Publications website at …

Detailed information about the X-ray structure determination and computational modeling (PDF)

X-ray crystallographic data (CIF) for complex **1**. CCDC 1994782 contains the supplementary crystallographic data for this paper. These data can be obtained free of charge from The Cambridge Crystallographic Data Centre via www.ccdc.cam.ac.uk/structures

■ **AUTHOR INFORMATION**
Corresponding Author

*machan@virginia.edu

*wag@caltech.edu

*tbg7h@virginia.edu

ORCID

Ana M. Geer: 0000-0003-1115-6759

Christopher Webber: 0000-0003-4299-3541

Robert J. Nielsen: 0000-0002-7962-0186

Diane A. Dickie: 0000-0003-0939-3309

Chang Liu: 0000-0002-7568-0608

Sen Zhang: 0000-0002-1716-3741

Charles W. Machan: 0000-0002-5182-1138

William A. Goddard, III: 0000-0003-0097-5716

T. Brent Gunnoe: 0000-0001-5714-3887

Notes

The authors declare no competing financial interest.

References

1. Agency, I. E., *World Energy Outlook 2018*. 2018.
2. Tsao, J. Y.; Schubert, E. F.; Fouquet, R.; Lave, M., The electrification of energy: Long-term trends and opportunities. *MRS Energy & Sustainability* **2018,** *5*, E7.
3. Lewis, N. S.; Nocera, D. G., Powering the planet: Chemical challenges in solar energy utilization. *Proc. Natl. Acad. Sci. U.S.A.* **2006,** *103* (43), 15729-15735.
4. Concepcion, J. J.; House, R. L.; Papanikolas, J. M.; Meyer, T. J., Chemical approaches to artificial photosynthesis. *Proc. Natl. Acad. Sci. U.S.A.* **2012,** *109* (39), 15560-15564.

5.   Zhang, B.; Sun, L., Artificial photosynthesis: opportunities and challenges of molecular catalysts. *Chem. Soc. Rev.* **2019,** *48* (7), 2216-2264.

6.   Matheu, R.; Garrido-Barros, P.; Gil-Sepulcre, M.; Ertem, M. Z.; Sala, X.; Gimbert-Suriñach, C.; Llobet, A., The development of molecular water oxidation catalysts. *Nat. Rev. Chem.* **2019,** *3* (5), 331-341.

7.   Betley, T. A.; Wu, Q.; Van Voorhis, T.; Nocera, D. G., Electronic Design Criteria for O−O Bond Formation via Metal−Oxo Complexes. *Inorg. Chem.* **2008,** *47* (6), 1849-1861.

8.   Ray, K.; Heims, F.; Schwalbe, M.; Nam, W., High-valent metal-oxo intermediates in energy demanding processes: from dioxygen reduction to water splitting. *Curr. Opin. Chem. Biol.* **2015,** *25*, 159-171.

9.   Yano, J.; Yachandra, V. K., Where Water Is Oxidized to Dioxygen: Structure of the Photosynthetic Mn_4Ca Cluster from X-ray Spectroscopy. *Inorg. Chem.* **2008,** *47* (6), 1711-1726.

10.   Askerka, M.; Brudvig, G. W.; Batista, V. S., The O_2-Evolving Complex of Photosystem II: Recent Insights from Quantum Mechanics/Molecular Mechanics (QM/MM), Extended X-ray Absorption Fine Structure (EXAFS), and Femtosecond X-ray Crystallography Data. *Acc. Chem. Res.* **2017,** *50* (1), 41-48.

11.   Yano, J.; Yachandra, V., Mn_4Ca Cluster in Photosynthesis: Where and How Water is Oxidized to Dioxygen. *Chem. Rev.* **2014,** *114* (8), 4175-4205.

12.   Cox, N.; Pantazis, D. A.; Neese, F.; Lubitz, W., Biological Water Oxidation. *Acc. Chem. Res.* **2013,** *46* (7), 1588-1596.

13.   Cox, N.; Retegan, M.; Neese, F.; Pantazis, D. A.; Boussac, A.; Lubitz, W., Electronic structure of the oxygen-evolving complex in photosystem II prior to O-O bond formation. *Science* **2014,** *345* (6198), 804.

14.   Cox, N.; Pantazis, D. A.; Neese, F.; Lubitz, W., Artificial photosynthesis: understanding water splitting in nature. *Interface Focus* **2015,** *5* (3), 20150009.

15.   Suen, N.-T.; Hung, S.-F.; Quan, Q.; Zhang, N.; Xu, Y.-J.; Chen, H. M., Electrocatalysis for the oxygen evolution reaction: recent development and future perspectives. *Chem. Soc. Rev.* **2017,** *46* (2), 337-365.

16.   Zahran, Z. N.; Tsubonouchi, Y.; Mohamed, E. A.; Yagi, M., Recent Advances in the Development of Molecular Catalyst-Based Anodes for Water Oxidation toward Artificial Photosynthesis. *ChemSusChem* **2019,** *12* (9), 1775-1793.

17.   Li, P.; Zhao, R.; Chen, H.; Wang, H.; Wei, P.; Huang, H.; Liu, Q.; Li, T.; Shi, X.; Zhang, Y.; Liu, M.; Sun, X., Recent Advances in the Development of Water Oxidation Electrocatalysts at Mild pH. *Small* **2019,** *15* (13), 1805103.

18.   Lloret-Fillol, J.; Costas, M., Chapter One - Water oxidation at base metal molecular catalysts. In *Adv. Organomet. Chem.*, Pérez, P. J., Ed. Academic Press: 2019; Vol. 71, pp 1-52.

19.   Zhang, Q.; Guan, J., Mono-/Multinuclear Water Oxidation Catalysts. *ChemSusChem* **2019,** *12* (14), 3209-3235.

20.   Blakemore, J. D.; Crabtree, R. H.; Brudvig, G. W., Molecular Catalysts for Water Oxidation. *Chem. Rev.* **2015,** *115* (23), 12974-13005.

21.   Kärkäs, M. D.; Verho, O.; Johnston, E. V.; Åkermark, B., Artificial Photosynthesis: Molecular Systems for Catalytic Water Oxidation. *Chem. Rev.* **2014,** *114* (24), 11863-12001.

22.   Kärkäs, M. D.; Åkermark, B., Water oxidation using earth-abundant transition metal catalysts: opportunities and challenges. *Dalton Trans.* **2016,** *45* (37), 14421-14461.

23.   Parent, A. R.; Sakai, K., Progress in Base-Metal Water Oxidation Catalysis. *ChemSusChem* **2014,** *7* (8), 2070-2080.

24.   Lukács, D.; Szyrwiel, Ł.; Pap, S. J., Copper Containing Molecular Systems in Electrocatalytic Water Oxidation—Trends and Perspectives. *Catalysts* **2019,** *9* (1).

25.   Lee, H.; Wu, X.; Sun, L., Copper-based homogeneous and heterogeneous catalysts for electrochemical water oxidation. *Nanoscale* **2020,** *12* (7), 4187-4218.

26.   Barnett, S. M.; Goldberg, K. I.; Mayer, J. M., A soluble copper–bipyridine water-oxidation electrocatalyst. *Nat. Chem.* **2012,** *4*, 498.

27.   Lu, C.; Du, J.; Su, X.-J.; Zhang, M.-T.; Xu, X.; Meyer, T. J.; Chen, Z., Cu(II) Aliphatic Diamine Complexes for Both Heterogeneous and Homogeneous Water Oxidation Catalysis in Basic and Neutral Solutions. *ACS Catal.* **2016,** *6* (1), 77-83.

28.   Fisher, K. J.; Materna, K. L.; Mercado, B. Q.; Crabtree, R. H.; Brudvig, G. W., Electrocatalytic Water Oxidation by a Copper(II) Complex of an Oxidation-Resistant Ligand. *ACS Catal.* **2017,** *7* (5), 3384-3387.

29.   Ghosh, T.; Ghosh, P.; Maayan, G., A Copper-Peptoid as a Highly Stable, Efficient, and Reusable Homogeneous Water Oxidation Electrocatalyst. *ACS Catal.* **2018,** *8* (11), 10631-10640.

30.   Chen, Z.; Meyer, T. J., Copper(II) Catalysis of Water Oxidation. *Angew. Chem., Int. Ed.* **2013,** *52* (2), 700-703.

31.   Coggins, M. K.; Zhang, M.-T.; Chen, Z.; Song, N.; Meyer, T. J., Single-Site Copper(II) Water Oxidation Electrocatalysis: Rate Enhancements with HPO_4^{2-} as a Proton Acceptor at pH 8. *Angew. Chem. Int. Ed.* **2014,** *53* (45), 12226-12230.

32.   Szyrwiel, Ł.; Lukács, D.; Ishikawa, T.; Brasun, J.; Szczukowski, Ł.; Szewczuk, Z.; Setner, B.; Pap, J. S., Electrocatalytic water oxidation influenced by the ratio between Cu^{2+} and a multiply branched peptide ligand. *Catal. Commun.* **2019,** *122*, 5-9.

33.   Pap, J. S.; Szyrwiel, Ł.; Srankó, D.; Kerner, Z.; Setner, B.; Szewczuk, Z.; Malinka, W., Electrocatalytic water oxidation by CuII complexes with branched peptides. *Chem. Commun.* **2015,** *51* (29), 6322-6324.

34.   Shen, J.; Wang, M.; Zhang, P.; Jiang, J.; Sun, L., Electrocatalytic water oxidation by copper(II) complexes containing a tetra- or pentadentate amine-pyridine ligand. *Chem. Commun.* **2017,** *53* (31), 4374-4377.

35.   Stott, L. A.; Prosser, K. E.; Berdichevsky, E. K.; Walsby, C. J.; Warren, J. J., Lowering water oxidation overpotentials using the ionisable imidazole of copper(2-(2'-pyridyl)imidazole). *Chem. Commun.* **2017,** *53* (3), 651-654.

36.   Yu, W.-B.; He, Q.-Y.; Ma, X.-F.; Shi, H.-T.; Wei, X., A new copper species based on an azo-compound utilized as a homogeneous catalyst for water oxidation. *Dalton Trans.* **2015,** *44* (1), 351-358.

37.   Nestke, S.; Ronge, E.; Siewert, I., Electrochemical water oxidation using a copper complex. *Dalton Trans.* **2018,** *47* (31), 10737-10741.

38.   Gerlach, D. L.; Bhagan, S.; Cruce, A. A.; Burks, D. B.; Nieto, I.; Truong, H. T.; Kelley, S. P.; Herbst-Gervasoni, C. J.; Jernigan, K. L.; Bowman, M. K.; Pan, S.; Zeller, M.; Papish, E. T., Studies of the Pathways Open to Copper Water Oxidation Catalysts Containing Proximal Hydroxy Groups During Basic Electrocatalysis. *Inorg. Chem.* **2014,** *53* (24), 12689-12698.

39.   Zhang, M.-T.; Chen, Z.; Kang, P.; Meyer, T. J., Electrocatalytic Water Oxidation with a Copper(II) Polypeptide Complex. *J. Am. Chem. Soc.* **2013,** *135* (6), 2048-2051.

40.   Zhang, T.; Wang, C.; Liu, S.; Wang, J.-L.; Lin, W., A Biomimetic Copper Water Oxidation Catalyst with Low Overpotential. *J. Am. Chem. Soc.* **2014,** *136* (1), 273-281.

41.   Garrido-Barros, P.; Funes-Ardoiz, I.; Drouet, S.; Benet-Buchholz, J.; Maseras, F.; Llobet, A., Redox Non-innocent Ligand Controls Water Oxidation Overpotential in a New Family of Mononuclear Cu-Based Efficient Catalysts. *J. Am. Chem. Soc.* **2015,** *137* (21), 6758-6761.

42.   Koepke, S. J.; Light, K. M.; VanNatta, P. E.; Wiley, K. M.; Kieber-Emmons, M. T., Electrocatalytic Water Oxidation by a Homogeneous Copper Catalyst Disfavors Single-Site Mechanisms. *J. Am. Chem. Soc.* **2017,** *139* (25), 8586-8600.

43.   Dong, H.; Du, J.; Kong, J.; He, X.; Chen, Z., Electrocatalytic Water Oxidation by Mononuclear Cu(II) Aliphatic Tetraamine Complexes. *ChemCatChem* **2019,** *11* (21), 5306-5312.

44.   Prevedello, A.; Bazzan, I.; Dalle Carbonare, N.; Giuliani, A.; Bhardwaj, S.; Africh, C.; Cepek, C.; Argazzi, R.; Bonchio, M.; Caramori, S.; Robert, M.; Sartorel, A., Heterogeneous and Homogeneous Routes in Water Oxidation Catalysis Starting from CuII Complexes with Tetraaza Macrocyclic Ligands. *Chem. Asian J.* **2016,** *11* (8), 1281-1287.

45.   Kuilya, H.; Alam, N.; Sarma, D.; Choudhury, D.; Kalita, A., Ligand assisted electrocatalytic water oxidation by a copper(II) complex in neutral phosphate buffer. *Chem. Commun.* **2019,** *55* (38), 5483-5486.

46.   Yu, F.; Li, F.; Hu, J.; Bai, L.; Zhu, Y.; Sun, L., Electrocatalytic water oxidation by a macrocyclic Cu(II) complex in neutral phosphate buffer. *Chem. Commun.* **2016,** *52* (68), 10377-10380.

47.   Kafentzi, M.-C.; Papadakis, R.; Gennarini, F.; Kochem, A.; Iranzo, O.; Le Mest, Y.; Le Poul, N.; Tron, T.; Faure, B.; Simaan, A. J.; Réglier, M., Electrochemical Water Oxidation and Stereoselective Oxygen Atom Transfer Mediated by a Copper Complex. *Chem. Eur. J.* **2018,** *24* (20), 5213-5224.

48.   Liu, Y.; Han, Y.; Zhang, Z.; Zhang, W.; Lai, W.; Wang, Y.; Cao, R., Low overpotential water oxidation at neutral pH catalyzed by a copper(II) porphyrin. *Chem. Sci.* **2019,** *10* (9), 2613-2622.

49.   Garrido-Barros, P.; Gimbert-Suriñach, C.; Matheu, R.; Sala, X.; Llobet, A., How to make an efficient and robust molecular catalyst for water oxidation. *Chem. Soc. Rev.* **2017,** *46* (20), 6088-6098.

50.   Sala, X.; Maji, S.; Bofill, R.; García-Antón, J.; Escriche, L.; Llobet, A., Molecular Water Oxidation Mechanisms Followed by Transition Metals: State of the Art. *Acc. Chem. Res.* **2014,** *47* (2), 504-516.

51.   Liu, F.; Concepcion, J. J.; Jurss, J. W.; Cardolaccia, T.; Templeton, J. L.; Meyer, T. J., Mechanisms of Water Oxidation from the Blue Dimer to Photosystem II. *Inorg. Chem.* **2008,** *47* (6), 1727-1752.

52.   Su, X.-J.; Gao, M.; Jiao, L.; Liao, R.-Z.; Siegbahn, P. E. M.; Cheng, J.-P.; Zhang, M.-T., Electrocatalytic Water Oxidation by a Dinuclear Copper Complex in a Neutral Aqueous Solution. *Angew. Chem. Int. Ed.* **2015,** *54* (16), 4909-4914.

53.   Su, X.-J.; Zheng, C.; Hu, Q.-Q.; Du, H.-Y.; Liao, R.-Z.; Zhang, M.-T., Bimetallic cooperative effect on O–O bond formation: copper polypyridyl complexes as water oxidation catalyst. *Dalton Trans.* **2018,** *47* (26), 8670-8675.

54.   Hu, Q.-Q.; Su, X.-J.; Zhang, M.-T., Electrocatalytic Water Oxidation by an Unsymmetrical Di-Copper Complex. *Inorg. Chem.* **2018,** *57* (17), 10481-10484.

55.   Edwards, S. J.; Soudackov, A. V.; Hammes-Schiffer, S., Analysis of Kinetic Isotope Effects for Proton-Coupled Electron Transfer Reactions. *J. Phys. Chem. A* **2009,** *113* (10), 2117-2126.

56.   Fang, T.; Fu, L.-Z.; Zhou, L.-L.; Zhan, S.-Z., A water-soluble dinuclear copper electrocatalyst, [Cu(oxpn)Cu(OH)$_2$] for both water reduction and oxidation. *Electrochim. Acta* **2015,** *161*, 388-394.

57.   Zhou, L.-L.; Fang, T.; Cao, J.-P.; Zhu, Z.-H.; Su, X.-T.; Zhan, S.-Z., A dinuclear copper(II) electrocatalyst both water reduction and oxidation. *J. Power Sources* **2015,** *273*, 298-304.

58.   Zhang, X.; Li, Y.-Y.; Jiang, J.; Zhang, R.; Liao, R.-Z.; Wang, M., A Dinuclear Copper Complex Featuring a Flexible Linker as Water Oxidation Catalyst with an Activity Far Superior to Its Mononuclear Counterpart. *Inorg. Chem.* **2020**.

59.   Wang, J.-M.; Liu, Y.-R.; Mao, X.-Y.; Shi, N.-N.; Zhang, X.; Wang, H.-S.; Fan, Y.-H.; Wang, M., Two Trinuclear CuII Complexes: Effect of Phosphonate Ligand on the Magnetic Property and Electrocatalytic Reactivity for Water Oxidation. *Chem. Asian J.* **2019,** *14* (15), 2685-2693.

60.   Li, T.-T.; Zheng, Y.-Q., Electrocatalytic water oxidation using a chair-like tetranuclear copper(II) complex in a neutral aqueous solution. *Dalton Trans.* **2016,** *45* (32), 12685-12690.

61.   Praneeth, V. K. K.; Kondo, M.; Woi, P. M.; Okamura, M.; Masaoka, S., Electrocatalytic Water Oxidation by a Tetranuclear Copper Complex. *ChemPlusChem* **2016,** *81* (10), 1123-1128.

62.   Jiang, X.; Li, J.; Yang, B.; Wei, X.-Z.; Dong, B.-W.; Kao, Y.; Huang, M.-Y.; Tung, C.-H.; Wu, L.-Z., A Bio-inspired Cu$_4$O$_4$ Cubane: Effective Molecular Catalysts for Electrocatalytic Water Oxidation in Aqueous Solution. *Angew. Chem. Int. Ed.* **2018,** *57* (26), 7850-7854.

63.   Gao, W.-S.; Wang, J.-M.; Shi, N.-N.; Chen, C.-N.; Fan, Y.-H.; Wang, M., Electrocatalytic water oxidation studies of a tetranuclear Cu(II) complex with cubane-like core $Cu_4(\mu^3\text{-}O)_4$. *New J. Chem.* **2019,** *43* (11), 4640-4647.

64.   Brezicki, G.; Kammert, J. D.; Gunnoe, T. B.; Paolucci, C.; Davis, R. J., Insights into the Speciation of Cu in the Cu-H-Mordenite Catalyst for the Oxidation of Methane to Methanol. *ACS Catal.* **2019,** *9* (6), 5308-5319.

65.   Pappas, D. K.; Martini, A.; Dyballa, M.; Kvande, K.; Teketel, S.; Lomachenko, K. A.; Baran, R.; Glatzel, P.; Arstad, B.; Berlier, G.; Lamberti, C.; Bordiga, S.; Olsbye, U.; Svelle, S.; Beato, P.; Borfecchia, E., The Nuclearity of the Active Site for Methane to Methanol Conversion in Cu-Mordenite: A Quantitative Assessment. *J. Am. Chem. Soc.* **2018,** *140* (45), 15270-15278.

66.   Ipek, B.; Wulfers, M. J.; Kim, H.; Göltl, F.; Hermans, I.; Smith, J. P.; Booksh, K. S.; Brown, C. M.; Lobo, R. F., Formation of $[Cu_2O_2]^{2+}$ and $[Cu_2O]^{2+}$ toward C–H Bond Activation in Cu-SSZ-13 and Cu-SSZ-39. *ACS Catal.* **2017,** *7* (7), 4291-4303.

67.   Grundner, S.; Markovits, M. A. C.; Li, G.; Tromp, M.; Pidko, E. A.; Hensen, E. J. M.; Jentys, A.; Sanchez-Sanchez, M.; Lercher, J. A., Single-site trinuclear copper oxygen clusters in mordenite for selective conversion of methane to methanol. *Nat. Commun.* **2015,** *6* (1), 7546.

68.   Suh, M. P.; Han, M. Y.; Lee, J. H.; Min, K. S.; Hyeon, C., One-Pot Template Synthesis and Properties of a Molecular Bowl: Dodecaaza Macrotetracycle with μ^3-Oxo and μ^3-Hydroxo Tricopper(II) Cores. *J. Am. Chem. Soc.* **1998,** *120* (15), 3819-3820.

69.   Thammavongsy, Z.; Mercer, I. P.; Yang, J. Y., Promoting proton coupled electron transfer in redox catalysts through molecular design. *Chem. Commun.* **2019,** *55* (70), 10342-10358.

70.   Yoon, J.; Mirica, L. M.; Stack, T. D. P.; Solomon, E. I., Variable-Temperature, Variable-Field Magnetic Circular Dichroism Studies of Tris-Hydroxy- and μ_3-Oxo-Bridged Trinuclear Cu(II) Complexes: Evaluation of Proposed Structures of the Native Intermediate of the Multicopper Oxidases. *J. Am. Chem. Soc.* **2005,** *127* (39), 13680-13693.

71.   Yoon, J.; Solomon, E. I., Ground-State Electronic and Magnetic Properties of a μ3-Oxo-Bridged Trinuclear Cu(II) Complex: Correlation to the Native Intermediate of the Multicopper Oxidases. *Inorg. Chem.* **2005,** *44* (22), 8076-8086.

72.   Appel, A. M.; Helm, M. L., Determining the Overpotential for a Molecular Electrocatalyst. *ACS Catal.* **2014,** *4* (2), 630-633.

73.   Lee, K. J.; McCarthy, B. D.; Dempsey, J. L., On decomposition, degradation, and voltammetric deviation: the electrochemist's field guide to identifying precatalyst transformation. *Chem. Soc. Rev.* **2019,** *48* (11), 2927-2945.

74.   Aksu, S., Electrochemical Equilibria of Copper in Aqueous Phosphoric Acid Solutions. *J. Electrochem. Soc.* **2009,** *156* (11), C387.

75.   Bard, A. J.; Faulkner, L. R., *Electrochemical Methods: Fundamentals and Applications, 2nd ed.* John Wiley & Sons, Inc.: Hoboken, NJ, 2001.

76.   McKinnon, M.; Rochford, J., Chapter 3.20 - Principles of Electrocatalysis. In *Green Chem.*, Török, B.; Dransfield, T., Eds. Elsevier: 2018; pp 695-727.

77.   Costentin, C.; Robert, M.; Savéant, J.-M., Catalysis of the electrochemical reduction of carbon dioxide. *Chem. Soc. Rev.* **2013,** *42* (6), 2423-2436.

78.   Garrido-Barros, P.; Moonshiram, D.; Gil-Sepulcre, M.; Pelosin, P.; Gimbert-Suriñach, C.; Benet-Buchholz, J.; Llobet, A., Redox Metal–Ligand Cooperativity Enables Robust and Efficient Water Oxidation Catalysis at Neutral pH with Macrocyclic Copper Complexes. *J. Am. Chem. Soc.* **2020,** *142* (41), 17434-17446.

79.   Han, Y.; Wu, Y.; Lai, W.; Cao, R., Electrocatalytic Water Oxidation by a Water-Soluble Nickel Porphyrin Complex at Neutral pH with Low Overpotential. *Inorg. Chem.* **2015,** *54* (11), 5604-5613.

80.   Zhang, L.-H.; Yu, F.; Shi, Y.; Li, F.; Li, H., Base-enhanced electrochemical water oxidation by a nickel complex in neutral aqueous solution. *Chem. Commun.* **2019,** *55* (43), 6122-6125.

81.   Shahadat, H. M.; Younus, H. A.; Ahmad, N.; Rahaman, M. A.; Khattak, Z. A. K.; Zhuiykov, S.; Verpoort, F., Homogenous electrochemical water oxidation by a nickel(II) complex based on a macrocyclic N-heterocyclic carbene/pyridine hybrid ligand. *Catal. Sci. Technol.* **2019,** *9* (20), 5651-5659.

82.   Wang, D.; Groves, J. T., Efficient water oxidation catalyzed by homogeneous cationic cobalt porphyrins with critical roles for the buffer base. *Proc. Natl. Acad. Sci. U.S.A.* **2013,** *110* (39), 15579–15584.

83.   Chen, Z.; Concepcion, J. J.; Hu, X.; Yang, W.; Hoertz, P. G.; Meyer, T. J., Concerted O atom–proton transfer in the O—O bond forming step in water oxidation. *Proc. Natl. Acad. Sci. U.S.A.* **2010,** *107* (16), 7225–7229.

84.   Ullman, A. M.; Liu, Y.; Huynh, M.; Bediako, D. K.; Wang, H.; Anderson, B. L.; Powers, D. C.; Breen, J. J.; Abruña, H. D.; Nocera, D. G., Water Oxidation Catalysis by Co(II) Impurities in Co(III)4O4 Cubanes. *J. Am. Chem. Soc.* **2014,** *136* (50), 17681-17688.

85.   Yi, Y.; Weinberg, G.; Prenzel, M.; Greiner, M.; Heumann, S.; Becker, S.; Schlögl, R., Electrochemical corrosion of a glassy carbon electrode. *Catal. Today* **2017,** *295*, 32-40.

86.   Kon, H., Parmagnetic resonance of molecular oxygen in condensed phases. *J. Am. Chem. Soc.* **1973,** *95* (4), 1045-1049.

87.   McAlpin, J. G.; Surendranath, Y.; Dincă, M.; Stich, T. A.; Stoian, S. A.; Casey, W. H.; Nocera, D. G.; Britt, R. D., EPR Evidence for Co(IV) Species Produced During Water Oxidation at Neutral pH. *J. Am. Chem. Soc.* **2010,** *132* (20), 6882-6883.

88.   Sekretaryova, A.; Jones, S. M.; Solomon, E. I., O2 Reduction to Water by High Potential Multicopper Oxidases: Contributions of the T1 Copper Site Potential and the Local Environment of the Trinuclear Copper Cluster. *J. Am. Chem. Soc.* **2019,** *141* (28), 11304-11314.

89.   Ping, Y.; Nielsen, R. J.; Goddard, W. A., The Reaction Mechanism with Free Energy Barriers at Constant Potentials for the Oxygen Evolution Reaction at the IrO2 (110) Surface. *J. Am. Chem. Soc.* **2017,** *139* (1), 149-155.

90.   Xiao, H.; Shin, H.; Goddard, W. A., Synergy between Fe and Ni in the optimal performance of (Ni,Fe)OOH catalysts for the oxygen evolution reaction. *Proc. Natl. Acad. Sci. U.S.A.* **2018,** *115* (23), 5872.

91.   Huang, L.-a.; Shin, H.; Goddard, W. A.; Wang, J., Photochemically deposited Ir-doped NiCo oxyhydroxide nanosheets provide highly efficient and stable electrocatalysts for the oxygen evolution reaction. *Nano Energy* **2020,** *75*, 104885.

92.   Liu, C.; Qian, J.; Ye, Y.; Zhou, H.; Sun, C.-J.; Sheehan, C.; Zhang, Z.; Wan, G.; Liu, Y.-S.; Guo, J.; Li, S.; Shin, H.; Hwang, S.; Gunnoe, T. B.; Goddard, W. A.; Zhang, S., Oxygen evolution reaction over catalytic single-site Co in a well-defined brookite TiO2 nanorod surface. *Nat. Catal.* **2021,** *4* (1), 36-45.

93.   Sheldrick, G., SHELXT - Integrated space-group and crystal-structure determination. *Acta Cryst. A* **2015,** *71* (1), 3-8.

94.   Dolomanov, O. V.; Bourhis, L. J.; Gildea, R. J.; Howard, J. A. K.; Puschmann, H., OLEX2: a complete structure solution, refinement and analysis program. *J. Appl. Crystallogr.* **2009,** *42* (2), 339-341.

95.   Spek, A., PLATON SQUEEZE: a tool for the calculation of the disordered solvent contribution to the calculated structure factors. *Acta Crystallogr. C* **2015,** *71* (1), 9-18.

96.   Bochevarov, A. D.; Harder, E.; Hughes, T. F.; Greenwood, J. R.; Braden, D. A.; Philipp, D. M.; Rinaldo, D.; Halls, M. D.; Zhang, J.; Friesner, R. A., Jaguar: A high-performance quantum chemistry software program with strengths in life and materials sciences. *Int. J. Quantum Chem* **2013,** *113* (18), 2110-2142.

97.   Becke, A. D., Density-functional thermochemistry. III. The role of exact exchange. *J. Chem. Phys.* **1993,** *98* (7), 5648-5652.

98.   Grimme, S.; Antony, J.; Ehrlich, S.; Krieg, H., A consistent and accurate ab initio parametrization of density functional dispersion correction (DFT-D) for the 94 elements H-Pu. *J. Chem. Phys.* **2010,** *132* (15), 154104.

99.   Hariharan, P. C.; Pople, J. A., The influence of polarization functions on molecular orbital hydrogenation energies. *Theor. Chim. Acta* **1973,** *28* (3), 213-222.

100.   Hehre, W. J.; Ditchfield, R.; Pople, J. A., Self—Consistent Molecular Orbital Methods. XII. Further Extensions of Gaussian—Type Basis Sets for Use in Molecular Orbital Studies of Organic Molecules. *J. Chem. Phys.* **1972,** *56* (5), 2257-2261.

101.   Roy, L. E.; Hay, P. J.; Martin, R. L., Revised Basis Sets for the LANL Effective Core Potentials. *J. Chem. Theory Comput.* **2008,** *4* (7), 1029-1031.

102.   Kahn, L. R.; Goddard, W. A., Ab Initio Effective Potentials for Use in Molecular Calculations. *J. Chem. Phys.* **1972,** *56* (6), 2685-2701.

103.   Zhao, Y.; Truhlar, D. G., The M06 suite of density functionals for main group thermochemistry, thermochemical kinetics, noncovalent interactions, excited states, and transition elements: two new functionals and systematic testing of four M06-class functionals and 12 other functionals. *Theor. Chem. Acc.* **2008,** *120* (1), 215-241.

104.   Friedrichs, M.; Zhou, R.; Edinger, S. R.; Friesner, R. A., Poisson–Boltzmann Analytical Gradients for Molecular Modeling Calculations. *J. Phys. Chem. B* **1999,** *103* (16), 3057-3061.

105.   Christensen, J. H.; Smith, A. J.; Reed, R. B.; Elmore, K. L., Dielectric Properties of Phosphoric Acid Solutions at 25° C. *J. Chem. Eng. Data* **1966,** *11* (1), 60-63.